Recognition mechanism of oxysterol binding protein by VAMP-associated protein-A revealed by NMR spectroscopy

（NMR による VAMP-associated protein-A の oxysterol binding protein 認識機構の研究）

古板　恭子
奈良先端科学技術大学院大学
バイオサイエンス研究科　生体高分子構造学講座
（箱嶋　敏雄　教授）

平成２２年３月２日提出

Contents

1. General introduction

Interactions of proteins with other macromolecules (proteins and nucleic acids) are fundamental to many biological processes. It is generally assumed that the function of a protein is linked to its tertiary structure. Biomolecular recognition processes are often described as the association of folded proteins that dock as rigid bodies (the "lock and key" mechanism) (Fischer, E., 1894), or as formation of an encounter complex that undergoes local conformational changes to optimize the initial interactions (the "induced fit" mechanism) (Koshland, D.E.J., 1958). These models have been proposed by comparing the three-dimensional structures of the bound and unbound proteins. Recently, however, it has been recognized that numerous proteins lack their intrinsic tertiary structures or contain long disordered segments (> 30-40 residues) under physiological conditions (Wright P.E. and Dyson H.J., 1999; Fink, A.L., 2005). Such proteins are referred to as intrinsically disordered proteins (IDPs), and frequently involved in regulatory functions in the cell through association with other molecules (Garza, A.S. *et. al.*, 2009). Larger interaction surfaces and structural plasticity in the native state is thought to be advantageous for IDPs in recognizing various targets with sufficient specificity, but without huge loss of affinity. On the target recognition of IDPs, two scenarios, "coupled folding and binding" and "conformation selection", have been suggested (Espinoza-Fonseca,L.M., 2009; Wright P.E. and Dyson H.J., 2009). In the coupled folding and binding model, IDP starts to change its conformation upon binding to its target, while the conformation selection model assumes that a structure similar to the bound conformation is more populated in a free state and chosen to form a complex. Supporting evidences for each model have been reported mainly from computer simulations, and experimental data using biophysical tools are limited in number.

NMR spectroscopy is one of powerful experimental tools to study molecular

recognition. It can provide not only three-dimensional structures of folded macromolecules, but also insights into unfolded states of macromolecules and low populated states of macromolecules present in the conformational ensemble. Therefore, NMR is useful for the study of molecular recognitions of both folded and unfolded macromolecules.

Here, we studied molecular recognition mechanism processes using NMR spectroscopy. In the main part of this thesis, the recognition mechanism of oxisterol binding protein (OSBP) by VAMP-associated membrane protein-A (VAP-A) is described. It was studied by NMR structure analysis of the complex between OSBP and VAP-A combined with NMR relaxation and titration, isothermal titration calorimetry and mutagenesis experiments. In Appendix, recognition mechanism of DNA by high-mobility group box 1 is described. It was investigated by NMR structure analyses of two artificial DNA oligomers which possess ethylene or propylene linkages.

2. Recognition mechanism of oxysterol binding protein by VAMP-associated protein-A

2.1 Introduction

Lipids are a major component of cell membranes and also act as signaling factors. A variety of cytosolic lipid binding proteins are involved in lipid signal transduction and lipid transport (Yang, H., 2006). Since the endoplasmic reticulum (ER) membrane is a major site for lipid biosyntheses, many cytosolic lipid binding proteins are localized at the ER membrane in order to play their roles. Oxysterol binding protein (OSBP) is a cytosolic receptor of cholesterol and oxysterols, such as 25-hydroxycholesterol (25-HC), and has been implicated to play a role in vesicle transport, lipid metabolism and signal transduction (Lehto, M. *et. al*., 2003, Wang, P.Y. *et. al.*, 2005). Wyles *et al*. showed that OSBP is localized at the cytosolic surface of the ER membrane by interacting with integral ER protein VAMP-associated protein (VAP-A), and identified the region of OSBP required for binding to VAP-A (Wyles, J.P. *et. al*., 2002). Shortly thereafter, Loewen *et al*. found that the sequence EFFDAxE is shared by the region of OSBP required for binding to VAP-A and the region of Osh1p (a yeast OSBP homologue) required for ER targeting. That sequence is conserved in many other lipid binding proteins and a transcriptional regulator specific to phospholipid synthesis, and acts as an ER targeting determinant through the interaction with VAP (Loewen, C.J. *et. al*., 2003). According to Loewen *et. al.*, 17 eukaryotic proteins contain the EFFDAxE sequence, at least 13 homologues of these proteins contain sequences closely related to EFFDAxE, and most of these EFFDAxE sequences or sequences closely related to EFFDAxE have acidic flanking regions (Loewen, C.J. *et. al*., 2003). The EFFDAxE sequence and sequences closely related to EFFDAxE are referred to as FFAT motifs since they consist of two phenylalanines (FF) in an acidic tract (AT). FFAT motifs in some lipid binding proteins

play a role in targeting to the ER (Wyles, J.P. *et. al.*, 2004, Amarilio, R *et. al*., 2005, Kawano, M. *et. al.*, 2006).

VAPs are type II membrane proteins which are conserved from yeast to human (Weir, M.L. *et. al*., 1998). Three VAP isoforms have been identified for human; VAP-A, VAP-B and VAP-C (a splicing variant of VAP-B) (Nishimura, Y. *et. al.*, 1999). VAPs are generally localized at the ER, although they can be localized at the nuclear membrane, golgi apparatus, tight junction or microtubules in some species and cell types (Lapierre, L.A. *et. al.*, 1999, Skehel, P.A. *et. al.*, 2000, Weir, M.L. *et. al*., 2001, Pennetta, G.. *et. al.*, 2002, Brickner, J.H., and Walter, P., 2004, Gao, L. *et. al.*, 2004). Most VAPs comprise three domains; a major sperm protein (MSP) domain, a coiled-coil domain and a transmembrane (TM) domain (Figure 1). VAPs bind to FFAT motifs using the MSP domain. VAPs are involved in a diverse range of cellular events. Prior to discovery of the FFAT motif, VAPs were mainly considered to play a role in vesicle trafficking given that VAPs were shown to interact with proteins involved in vesicular fusion, although the details of their functions were unclear (Skehel, P.A. *et. al*., 1995; Soussan, L., *et. al*., 1999; Foster, L.J. *et. al.*, 2000; Weir, M.L. *et. al*., 2001). Following discovery of the FFAT motif, VAPs were shown to play important roles in non-vesicular lipid transport (Kawano, M. *et. al.*, 2006), lipid metabolism (Loewen, C.J. *et. al*., 2004), ER structure regulation (Amarilio, R. *et. al*., 2005; Kaiser, S.E. *et. al*., 2005) and unfolded protein responses (Brickner, J.H., and Walter, P, 2004) through interaction with FFAT motifs. Additionally, the P56S mutation in human VAP-B causes autosomal dominant motoneuronal diseases, familial amyotrophic lateral sclerosis 8 (ALS8), and P56S mutants of human VAP-B form aggregations in cells (Nishimura, A.L. *et. al.*, 2004; Kanekura, K. *et. al.*, 2006).

OSBP, which was the first lipid binding protein shown to interact with VAP-A, requires the interaction of the FFAT motif with VAP-A to perform its function. In addition to the

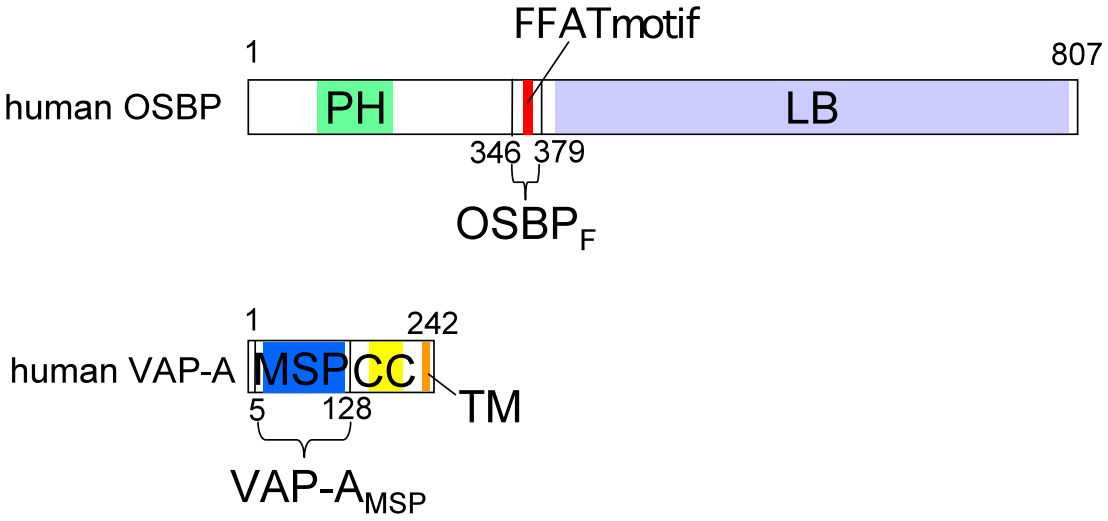

Figure 1. Domain structures of human OSBP and human VAP-A. Regions used in this study are indicated under each figure. Abbreviations: MSP, major sperm protein; CC, coiled-coil; TM, transmembrane; PH, pleckstrin homology; LB, lipid binding.

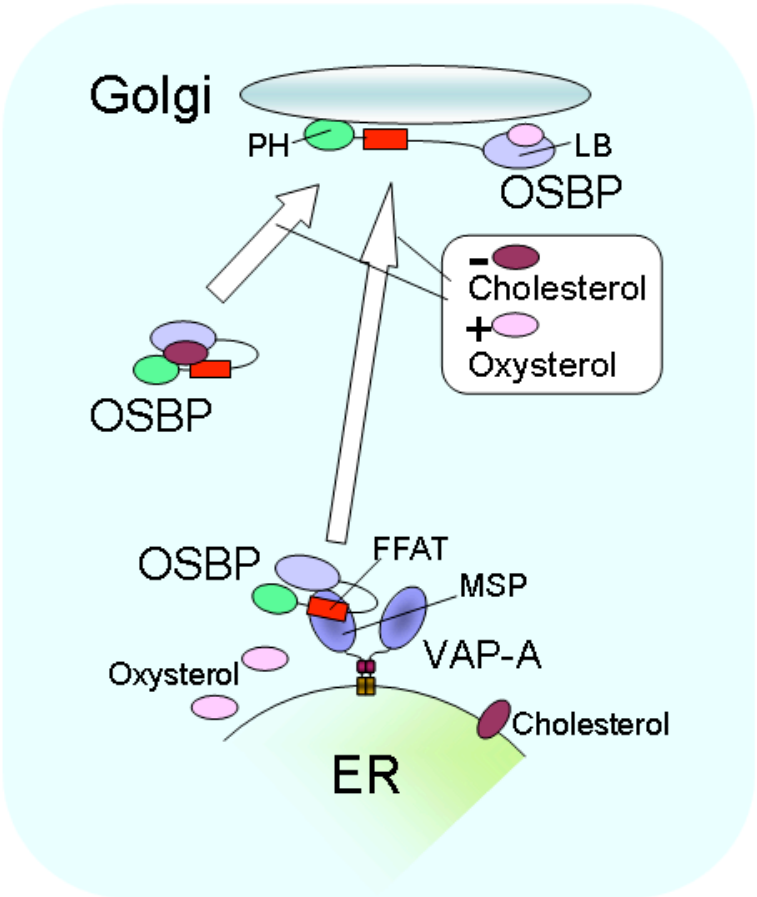

Figure 2. Sub-cellular localization of OSBP.

FFAT motif, OSBP has an N-terminal pleckstrin homology (PH) domain and a C-terminal lipid binding domain (Figure 1). The PH domain of OSBP binds to the Golgi apparatus by interacting phosphatidylinositol 4 phospates and Golgi GTPase ARF (Levin, T.P. and Munro, S., 2002). OSBP is usually localized in a vesicular compartment and the cytosol, and translocates to the Golgi apparatus surface in response to increases in cellular 25-HC or depletion of cellular cholesterol (Figure 2) (Ridgway, N.D. *et. al*., 1992). 25-HC stimulates sphingomyelin synthesis (Ridgway, N.D., 1995), and the interaction between the FFAT motif of OSBP and VAP-A is essential for stimulation of sphingomyelin synthesis by 25-HC (Perry, R.J. and Ridgway, N.D., 2006). Proteins displaying homology to the C-terminal lipid binding domain of OSBP are referred to as OSBP-related proteins (ORPs) (Jaworski, C.J., 2001; Lehto, M. *et. al*., 2003; Olkkonen, V.M. *et. al*., 2006). Humans possess 12 ORP genes including OSBP (Lehto, M., *et. al*., 2001). Four of the 12 human ORPs contain the EFFDAxE sequence (OSBP and ORP3, 6 and 7), and 4 contain sequences closely related to EFFDAxE (ORP1, 2, 4 and 9). In addition to these 8 human ORPs, human lipid binding proteins containing FFAT motifs (Figure 3) have been investigated with respect to their interaction with VAPs and subcellular localization (Table 1). According to these studies, ORP4 and ORP9 bind strongly to VAPs, although they do not contain the EFFDAxE sequence. On the other hand, ORP3, which contains EFFDAxE sequence, shows only weak binding to VAP. These results suggest that the EFFDAxE sequence alone is not sufficient for strong binding to VAP, and crucial residues may be present in regions other than the EFFDAxE sequence. An X-ray structure of the complex between the rat VAP-A MSP domain and a rat ORP1 fragment containing the FFAT motif have been determined (Kaiser, S.E. *et. al*., 2005). However, the ORP1 fragment used in the X-ray structure analysis does not contain the FFAT motif consensus sequence (EFFDAxE), and the length is short (10 residues including the FFAT motif). This X-ray structure is not consistent with some biochemical and mutation results

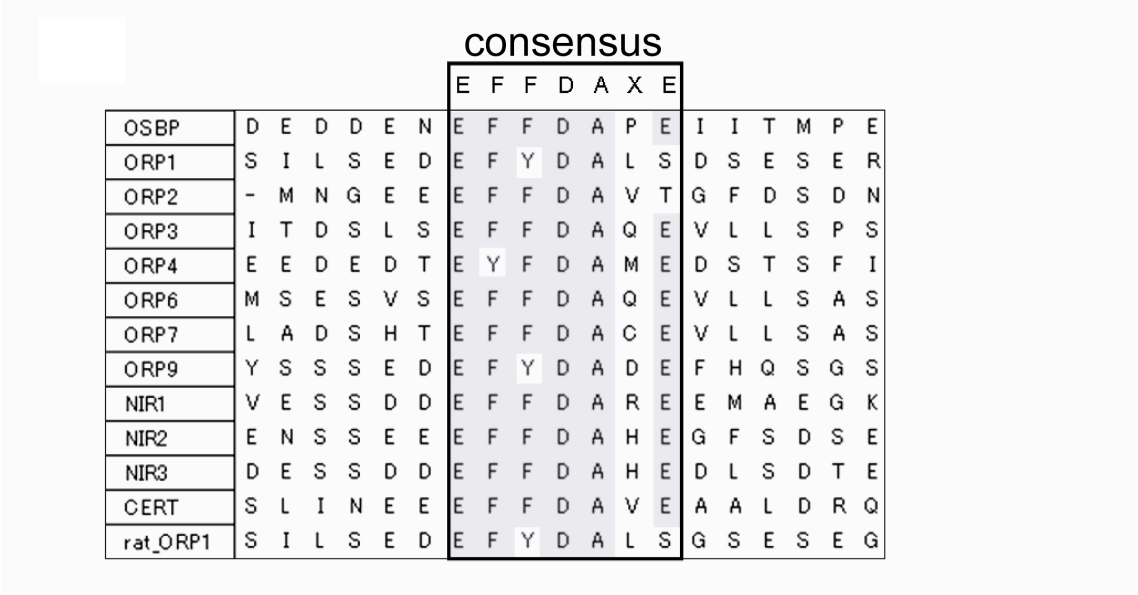

Figure 3. Alignment of FFAT motifs of human lipid binding proteins and rat ORP1.

Table 1. Summary of binding assays of VAP and human proteins containing FFAT motifs. PDA, GST pull down assay; Y2H, yeast two hybrid; IP, coimmunoprecipitation; S, strong binding; W, weak binding; n.d., no data; ○, the protein binds to VAP or localizes at ER; ×, the protein does not bind to VAP, or does not localize at ER.

	PDA[a]	Y2H	IP	ER localization
OSBP	S	○[b]	○[b]	○*, [b]
ORP1	W	n.d.	n.d.	×[e]
ORP2	W	n.d.	n.d.	×[e]
ORP3	W	n.d.	n.d.	○[f]
ORP4	S	n.d.	n.d.	×[g]
ORP6	S	n.d.	n.d.	○[f]
ORP7	S	n.d.	n.d.	○[f]
ORP9	S	○[a]	n.d.	○ *, [a]
NIR1	n.d.	n.d.	○[c]	×[c]
NIR2	n.d.	n.d.	○[c]	○**, [c]
NIR3	n.d.	n.d.	○[c]	○**, [c]
CERT	n.d.	n.d.	○[d]	○**, [d]

* overexpression of protein containing a FFAT motif; ** coexpression of VAP and protein containing a FFAT motif; [a] (Wyles, J. P. and Ridgway, N. D., 2004); [b] (Wyles, J. P. *et. al*., 2002); [c] (Amarilio, R. *et. al.*, 2005); [d] (Kawano, M. *et. al*., 2006); [e] (Xu, Y. *et. al*., 2001); [f] (Lehto, M. *et. al.*, 2004), [g] (Wang, C. *et. al.*, 2002).

(Loewen, C.J. *et. al*., 2003; Kaiser, S.E. et. al., 2005; Kawano, M. *et. al.*, 2006). Therefore, details of the interaction between OSBP and VAP-A remain unclear.

In this study, we have determined the solution structure of the complex between the human VAP-A MSP domain (VAP-A_{MSP}) and human OSBP fragment containing the FFAT motif ($OBSP_F$) (Figure 1) in an effort to delineate the interaction between VAP-A and OSBP. In order to examine the roles of residues around the FFAT motif, we used longer fragment (34 residues of the FFAT motif with 12 and 15 residues at the N- and C- terminal sides of the FFAT motif, respectively). The detailed binding mechanism was further investigated by NMR and isothermal titration calorimetry (ITC) combined with mutagenesis. We have successfully examined (1) the stoichiometry between VAP-A_{MSP} and $OSBP_F$, (2) the disorder property of $OSBP_F$, and (3) residues within and at the N-terminal side of the FFAT motif that contribute to the binding to VAP-A_{MSP}. Additionally, we have investigated the effect of the mutation which causes the disease ALS8 using NMR and differential scanning calorimetry (DSC).

2.2 Materials and Methods

2.2.1 Protein expression and purification

DNA fragments encoding VAP-A_{MSP} (human VAP-A E5-E128) and C-terminal hexa-histidine tagged $OSBP_F$ (human OSBP G346-S379) with an N-terminal tryptophan were amplified from QUICK-Clone™ cDNAs (CloneTech), and subsequently cloned into the pGEX-6P-3 expression vector modified in a PRESAT manner (Goda, N. *et al*, 2004). The protein and peptide were over-expressed in *E. coli* Rosetta (DE3). Unlabeled proteins were expressed in LB medium. $^{13}C/\ ^{15}N$-labeled, and ^{15}N-labeled proteins were expressed in M9 medium containing $^{15}NH_4Cl$ and ^{13}C glucose, or $^{15}NH_4Cl$ and unlabeled glucose, respectively.

Cells expressing VAP-A_{MSP} were lysed by sonication in a buffer solution containing 50 mM HEPES (pH 8.0), 300 mM KCl, 5 mM DTT and 0.1 mM EDTA. The lysate was centrifuged at 35,000 rpm for 30 min at 4 °C. The supernatant was loaded onto a glutathione Sepharose 4B resin (GE Healthcare), and VAP-A was eluted with a buffer solution containing 50 mM HEPES (pH 8.0), 300 mM KCl, 5 mM DTT, 0.1 mM EDTA and 10 mM glutathione. Fractions containing VAP-A_{MSP} were applied to a Superdex 75 (26/ 60) gel-filtration column (GE Healthcare) equilibrated with buffer containing 50 mM Tris-HCl (pH 7.6), 150 mM KCl, 0.1 mM EDTA and 5 mM DTT. Fractions containing VAP-A_{MSP} were concentrated and the GST tag was removed using PreScission Protease (GE Healthcare). Finally, The sample was applied to a Superdex 75 (26/ 60) gel filtration column (GE Healthcare) equilibrated with buffer containing 50 mM potassium phosphate (pH 6.9), 100 mM KCl, 0.1 mM EDTA and 1 mM DTT. Meanwhile, cells expressing $OSBP_F$ were lysed by sonication in a buffer containing 50 mM HEPES (pH 8.0), 300 mM KCl and 1 mM DTT. The lysate was centrifuged at 35,000 rpm for 30 min at 4°C. The supernatant was loaded onto a glutathione Sepharose 4B resin (GE Healthcare) and $OSBP_F$ was eluted with a buffer containing 50 mM HEPES (pH 7.5), 150 mM KCl, 1 mM DTT and 10 mM glutathione. Fractions containing $OSBP_F$ were concentrated and the GST tag was removed using PreScission Protease (GE Healthcare). The sample was then loaded onto a Ni-Sepharose resin (GE Healthcare) and $OSBP_F$ was eluted with a buffer containing 50 mM HEPES (pH 7.5), 50 mM KCl and 300 mM imidazole. Finally, the buffer was exchanged to 50 mM potassium phosphate (pH 6.9), 100 mM KCl, 0.1 mM EDTA and 1 mM DTT. Expression vectors for the site-directed mutants of $OSBP_F$ (E356K, E358A, F360A, E360Q, D361A, E364K and E356K/E364K) and VAP-A_{MSP} (P56S) were prepared using QuikChange (Stratagene). Unlabeled mutants $OSBP_F$ and ^{15}N-labeled P56S VAP-A_{MSP} were over-expressed in *E. coli* Rosetta (DE3). Then, proteins were purified using the same method as described above.

2.2.2 NMR samples

All NMR samples of the complex between VAP-A_{MSP} and $OSBP_F$ were 1.0 or 1.1 mM prepared in 93% H_2O / 7% D_2O (v/v) containing 50 mM potassium phosphate (pH 6.9), 100 mM KCl, 1 mM DTT and 0.1 mM EDTA. Six complexes were prepared: $^{13}C/^{15}N$ or ^{15}N-labeled VAP-A_{MSP} with unlabeled $OSBP_F$, unlabeled VAP-A_{MSP} with $^{13}C/^{15}N$ or ^{15}N-labeled $OSBP_F$, $^{13}C/^{15}N$-labeled VAP-A_{MSP} with $^{13}C/^{15}N$-labeled $OSBP_F$, and ^{15}N-labeled VAP-A_{MSP} with ^{15}N-labeled $OSBP_F$. Complex formation was monitored using the ^{15}N HSQC spectrum of the mixture of VAP-A_{MSP} and $OSBP_F$. Peak positions of the complex were identified by the ^{1}H-^{15}N Hetero-nuclear Single Quantum Coherence (HSQC) spectrum of ^{15}N-labeled VAP-A_{MSP} or ^{15}N-labeled $OSBP_F$ in the presence of an excess of unlabeled $OSBP_F$ or unlabeled VAP-A_{MSP}, respectively.

2.2.3 NMR experiments

All NMR experiments were performed using a Bruker AV500 or DRX800 spectrometer at 303 K. All spectra were processed using NMRpipe (Delaglio, F. *et. al.*, 1995) and analyzed using SPARKY (Goddard and Kneller, UCSF). For backbone resonance assignments of free VAP-A_{MSP}, free $OSBP_F$, and the complex, HNCACB, HN(CO)CACB, HN(CA)CO and HNCO spectra (Sattler, M.S. *et. al.*, 1999; Cavanagh, J. *et. al.*, 2007) of each $^{13}C/^{15}N$-labeled samples were recorded. Side chain resonances of the complex were made using C(CO)NH, H(CCO)NH, 4D-HC(CO)NH, HCCH-TOCSY, ^{15}N-edited TOCSY-HSQC and ^{5}N-filtered ^{1}H-^{1}H NOESY spectra (Sattler, M.S. *et. al.*, 1999; Cavanagh, J. *et. al.*, 2007). Distance restraints of the complex were obtained from the 3D ^{13}C-edited NOESY spectrum of $^{13}C/^{15}N$-labeled complex, 3D ^{15}N-edited NOESY and 2D ^{15}N-filtered ^{1}H-^{1}H NOESY spectra of ^{15}N-labeled complex, and ^{13}C-edited (F_2)/^{13}C-filtered (F_1) NOESY spectrum of the

complex between $^{13}C/^{15}N$-labeled VAP-A_{MSP} and unlabeled $OSBP_F$ (Sattler, M.S. *et. al.*, 1999; Cavanagh, J. *et. al.*, 2007). In order to obtain χ_1 angles, HNHB and HN(CO)HB spectra (Archer, S.J. *et. al.*, 1991; Grzesiek, S. *et. al*., 1992) and three bond $J_{C'C\gamma}$ and $J_{NC\gamma}$ couplings (Hu, J.S. *et. al.*, 1997) were measured.

The ^{15}N longitudinal spin-relaxation rates (R1) were measured with relaxation delays of 16.5*, 38.5, 60.5*, 115.5, 203.5, 335.5, 555.5 and 885.5 ms (Cavanagh, J. *et. al.*, 2007). The ^{15}N transverse relaxation rates (R2) were measured with relaxation delays of 16*, 32, 48*, 64, 96, 112 and 128 ms (Cavanagh, J. *et. al.*, 2007). In these measurements, time points marked with an asterisk were duplicated for error estimations. ^1H-^{15}N hetero NOEs were recorded with and without proton saturation in an interleaved fashion (Cavanagh, J. *et. al.*, 2007).

Titration experiments of ^{15}N-labeled VAP-A_{MSP} with unlabeled $OSBP_F$ (WT) were performed in 90% H_2O / 10% D_2O (v/v) containing 50 mM potassium phosphate (pH 6.9), 100 mM KCl, 1 mM DTT and 0.1 mM EDTA, and in 90 % H_2O / 10 % D_2O (v/v) containing 50 mM potassium phosphate (pH 6.9), 500 mM KCl, 1 mM DTT and 0.1 mM EDTA. Titration experiments of ^{15}N-labeled VAP-A_{MSP} with unlabeled $OSBP_F$ (E356K) was performed in 90% H_2O / 10% D_2O (v/v) containing 50 mM potassium phosphate (pH 6.9), 100 mM KCl, 1 mM DTT and 0.1 mM EDTA. For all titration experiments, the initial concentration of VAP-A_{MSP} was set to 0.17 mM. For the titration with $OSBP_F$ (WT), 3.17 mM $OSBP_F$ (WT) was added to VAP-A_{MSP} at molar ratios to VAP-A_{MSP} of 0.15, 0.30, 0.44, 0.59, 0.73, 0.88, 1.02, 1.17, 1.46 and 1.76. For the titration with $OSBP_F$ (E356K), 2.30 mM $OSBP_F$ (E356K) was added to VAP-A_{MSP} with molar ratios to VAP-A_{MSP} of 0.15, 0.30, 0.59, 0.88, 1.17, 1.46, 1.76, 2.34, 3.51 and 5.85. Finally, at 500 mM KCl, 1.69 mM $OSBP_F$ (WT) was added to VAP-A_{MSP} with molar ratios to VAP-A_{MSP} of 0.15, 0.30, 0.44, 0.59, 0.73, 0.88, 1.02, 1.17, 1.46, 2.34, 3.51, 5.85 and 10.5. For the line-shape analysis, the LineShapeKin Simulation 4.1.1 software (http://lineshapekin.net) (Kovrigin, E.L. and Loria, J.P., 2006) was

used with the following parameters; Ka = 2.8×10^5 M^{-1}, k_{off} = 20, 40, 80, 100, 120, 140, 160, 180, 200, 250, 300, 350, 400, 450, 500, 700, 1000 and 2000 s^{-1}, frequency for ^{15}N of Glu-91 = 40748 and 41237 s^{-1} for free and complex, respectively, R2 = 11 and 17 s^{-1} for free and complex, respectively, receptor concentration = 0.16-0.17 mM, and ligand/receptor ratio = 0.15, 0.30, 0.44, 0.59, 0.73, 0.88, 1.02, 1.17, 1.46 and 1.76.

2.2.4 ^{15}N relaxation analysis

All R1, R2 and ^1H-^{15}N hetero NOE values were measured using the AV500 spectrometer at 303K. Peak height intensities in each spectrum were measured using SPARKY. ^1H-^{15}N hetero NOE values were obtained by calculating the ratios of the peak height intensities in the spectra with and without ^1H saturation. For determination of the overall rotational correlation time (τ_C) of the complex, R1 and R2 values were obtained using the Sparky2rate software (Loria Lab, http://xbeams.chem.yale.edu/~loria), which employs a relaxation peak intensity file generated by Sparky and fits the rate constants using the nonlinear least-squares fitting program CURVEFIT (Palmer, A.G.. *et. al.*, 1991). Then, τ_C for the complex was calculated using the program TENSOR 2.0 (Dosset, P., *et. al*., 2000) assuming isotropic, axial symmetric and fully anisotropic motion, and the isotropic model was selected. For determination of the residue-specific order parameters (S^2) of VAP-A_{MSP} in the bound and unbound states, the exponential decay curves of R1 and R2 were fitted to a two-parameter exponential equation using in-house developed software. The uncertainties of the relaxation rates were estimated by 500 Monte-Carlo simulations using the intensity deviations of duplicated time points. Baseline noise levels were used for the uncertainties in hetero NOE experiments. Rotational diffusion tensors and Lipari-Szabo model-free analyses for VAP-A_{MSP} in the unbound and bound states were achieved using TENSOR 2.0 (Dosset, P., *et. al*., 2000). Only residues having values higher than 0.7 in the hetero NOE data were

considered for determination of the rotational diffusion tensor. Anisotropic and isotropic rotational diffusion tensors were assumed for the unbound and bound states of VAP-A_{MSP}, respectively. Using these tensors, S^2 were calculated.

2.2.5 Structure calculation

The NOE cross peaks in the 3D ^{13}C-edited (F2)/ ^{13}C-filtered (F1) NOESY spectrum were assigned manually, and 29 intermolecular upper distance limits were obtained. The NOE cross peaks in the 3D ^{13}C-edited NOESY, 3D ^{15}N-edited NOESY and ^{5}N-filtered ^{1}H-^{1}H NOESY spectra were assigned using the CANDID algorithm of CYANA (Herrmann, T. *et. al.*, 2002). A total of 2796 upper distance restraints were obtained by CANDID. 141 backbone torsion angle restraints were derived using the TALOS program (Cornilescu, G.. *et. al*., 1999), 10 χ_1 angle restraints were obtained from HNHB and HN(CO)HB spectra and 3 χ_1 angle restraints were obtained by three bond $J_{C'C\gamma}$ and $J_{NC\gamma}$ couplings. With these restraints, a total of 100 structures that did not show significant violations were generated by 20,000 time-step dynamics using CYANA (Guntert, P. *et. al*., 1997; Guntert, P., 2004), and these were further refined by AMBER 9 (Pearlman, D.A. *et. al.*, 1995) using an all-atom force field (ff99SB). The AMBER refinement consists of three stages: 1,500 steps of energy minimization, 20 ps molecular dynamics, and 1,500 steps of energy minimization. To approximate solvent effects, a generalized Born model (igb=5 and gbsa=1) was used (Onufriev, A. *et. al.*, 2004). The best 20 structures were selected and analyzed using AQUA and PROCHECK-NMR software (Laskowski, R.A. *et. al*., 1996). A structure closest to the lowest energy was employed as being representative.

2.2.6 Isothermal titration calorimetry (ITC)

Prior to the ITC experiments, purified protein and peptides were dialyzed against 50

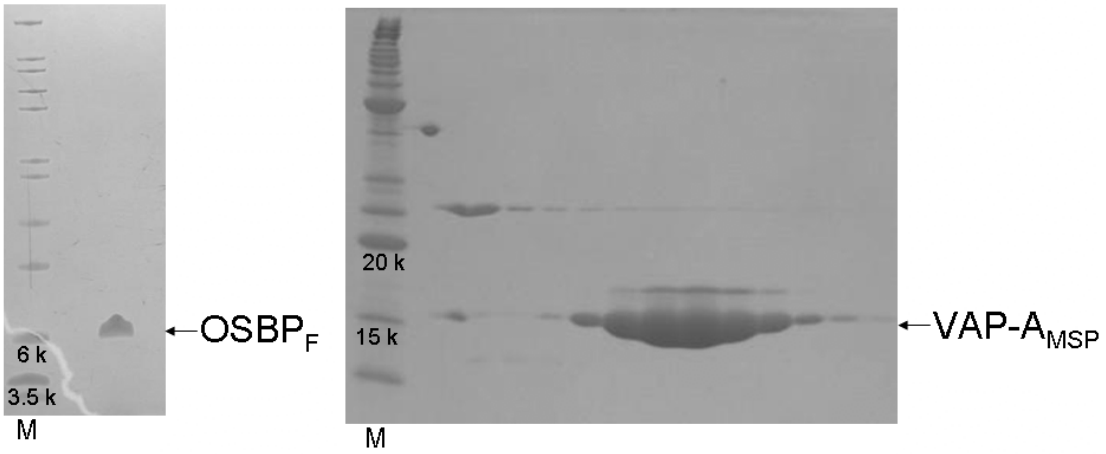

Figure 4. SDS-polyacrylamide gel electrophoresis of $OSBP_F$ and VAP-A_{MSP}.

mM potassium phosphate buffer (pH 6.9) containing 100 mM KCl, 1 mM DTT and 0.1 mM EDTA. This dialysis buffer was used to measure heats of dilution. ITC experiments were performed at 293 K on a VP-ITC or an Omega Micro Calorimeter (Microcal Inc). The experimental data were analyzed by employing the Origin-ITC software package. Heats of dilution were subtracted from the raw data prior to analysis.

The concentrations of $OSBP_F$ (WT and mutants) were determined by measuring the absorbance at 280 nm, while that of VAP-A_{MSP} was not determined accurately due to trace contamination with other proteins (Figure 4). From the ITC data analysis, the apparent stoichiometry was 1:1.17 for $OSBP_F$: VAP-A_{MSP}. Here, we have assumed that this difference (17%) is derived from an overestimation of the VAP-A_{MSP} concentration due to contamination, and therefore the concentration of VAP-A_{MSP} was re-calibrated for ITC data analyses for mutational studies.

2.2.7 Differential scanning calorimetry (DSC)

Prior to the DSC experiments, WT and P56S VAP-A_{MSP} were dialyzed against 50 mM potassium phosphate buffer (pH 6.9) containing 100 mM KCl, 1 mM DTT and 0.1 mM EDTA, and 50 mM potassium phosphate buffer (pH 6.9) containing 100 mM KCl and 1 mM DTT, respectively. The dialysate buffer was used as a reference solution for the DSC scan. Both calorimetric scans were performed using nanoDSC (Calorimetry Sciences Corp., Utah). WT (1.5 mg/ ml) and P56S (1.8 mg/ ml) were scanned from 273 to 353 K and from 273 to 343 K, respectively, with a heating rate of 1 K/min.

2.3 Results

2.3.1 Chemical shift assignments

All resonances of backbone nuclei (^{1}HN, ^{15}N, ^{13}Cα and ^{13}C') of the complex between VAP-A_{MSP} and $OSBP_F$ were assigned, and more than 90% of side chain ^{1}H and ^{13}C resonances of the complex were assigned (BMRB ID, 7025) using conventional triple-resonance techniques (Cavanagh, J. *et. al.*, 2007). Resonances of all backbone nuclei of free VAP-A_{MSP} and free $OSBP_F$ were also assigned using conventional triple-resonance techniques (Cavanagh, J. *et. al.*, 2007) except for $OSBP_F$ Ser-379 ^{13}C' and $^{13}C_{\alpha}$.

2.3.2 Stoichiometry between VAP-A_{MSP} and $OSBP_F$

Initially, the ITC experiment for the interaction of $OSBP_F$ and VAP-A_{MSP} was performed (Figure 5). From these results, the molar ratio of the complex is concluded to be 1:1. Then, the apparent molecular mass of the complex was then determined by NMR relaxation spectroscopy. From the R1, R2 and ^{1}H-^{15}N hetero NOE values, the τ_c value of the complex at 303 K was determined to be 12.6 ± 0.1 ns using TENSOR 2.0. Since the τ_c value of a globular protein is roughly proportional to the apparent MW, a linear correlation plot between τ_c and apparent molecular mass was given as shown in Figure 6. Experimentally determined τ_c values reported in the literature (Ryabov, Y.E. *et. al.*, 2006) were scaled to 303 K in Figure 6, assuming that τ_c value correlates with temperature as η(T)/T, where η(T) = $1.7753 - 0.0565\cdot(T - 273) + 1.0751 \times 10\text{-}3\cdot(T - 273)^2 - 9.2222 \times 10\text{-}6\cdot(T - 273)^3$ (Ryabov, Y. E. *et. al.*, 2006). The molecular masses were determined as described previously (Su X.C. *et. al.*, 2007), briefly, the molecular masses were determined from the amino acid sequences of the respective PDB files (Ryabov, Y.E. *et. al.*, 2006). Using these data, linear fit was performed using Origin 7 software (OriginLab corporation). According to Figure 6, the τ_c value of 12.6 ns indicates that the apparent molecular mass is between 19.6 and 32.2 kDa (95% accuracy). The molecular mass of the complex comprising of one VAP-A_{MSP} and one $OSBP_F$ is 20.2 kDa (VAP-A_{MSP}, 14.8 kDa; $OSBP_F$, 5.4 kDa). Therefore, the apparent

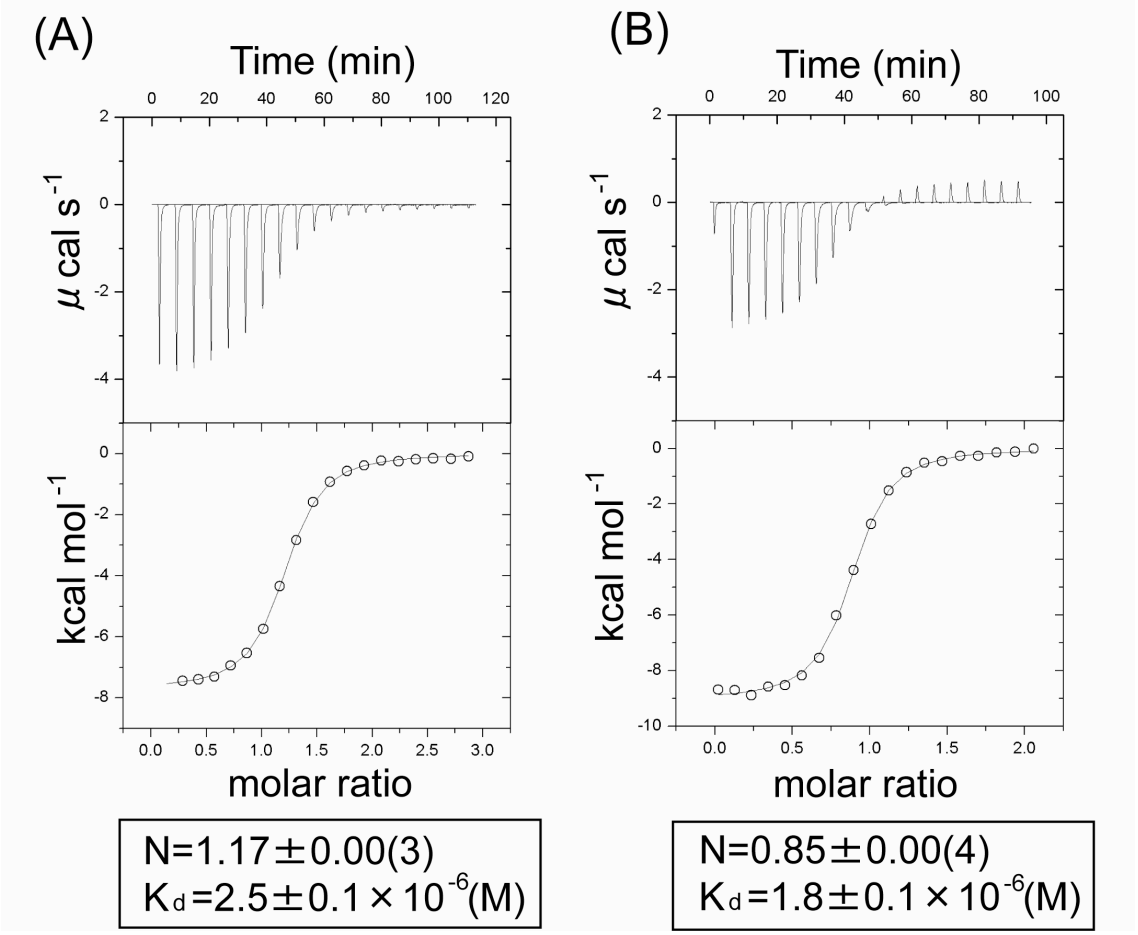

Figure 5. Data derived from the ITC experiment of $OSBP_F$ (0.1 mM) titrated with VAP-A_{MSP} (2.0 mM) (A) and VAP-A_{MSP} (0.1 mM) titrated with $OSBP_F$ (1.5 mM) (B). In (A), the titration experiments were performed with eighteen 10 μl injections into a 1.8 ml $OSBP_F$ solution. In (B), the titration experiments were performed with an initial 2 μl injection followed by eighteen 10-μl injections into a 1.8 ml VAP-A_{MSP} solution. The top panels show the raw data, while the middle panels show the integrated ITC curve obtained following subtraction of the heats of dilution. The experimental data were analyzed by employing the Origin-ITC software package using concentrations of VAP-A_{MSP} and $OSBP_F$ determined by measuring the absorbance at 280 nm. Stoichiometry (N) and dissociation constant (K_d) obtained from the data analyses are shown in the bottom panels. Assuming a 17% overestimation of VAP-A_{MSP} concentration (1.7 and 0.09 mM VAP-A_{MSP} instead of 2.0 and 0.1 mM, respectively), these two N values become 1.00 (± 0.01) with K_d value 1.8 (± 0.3) × 10^{-6} M.

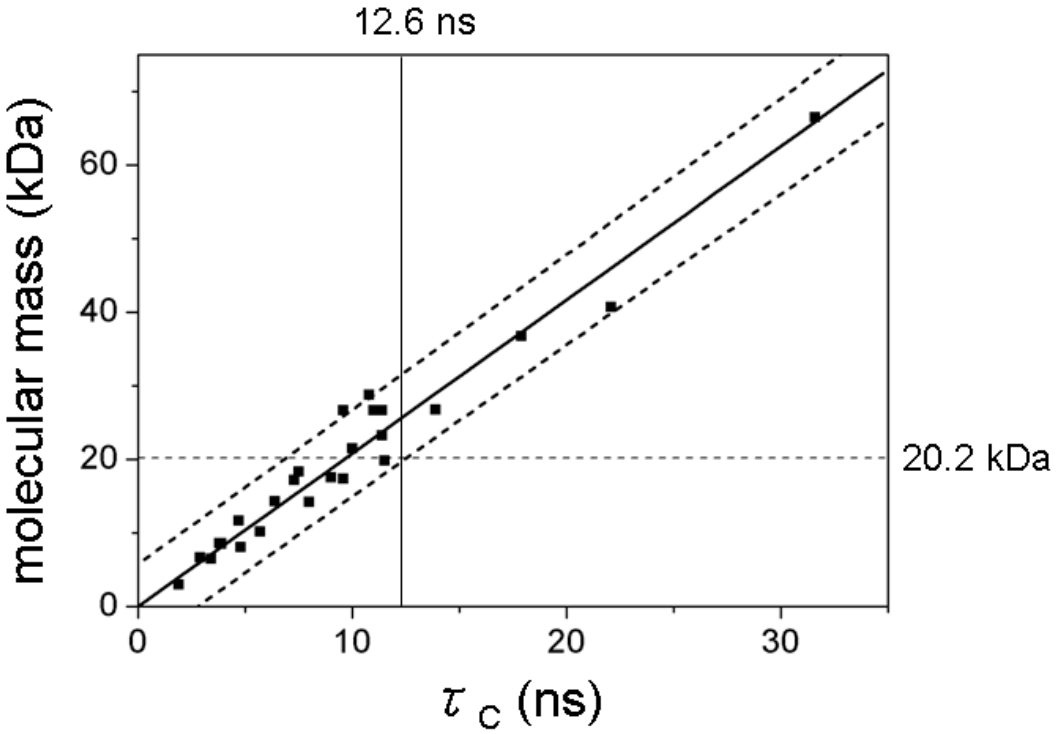

Figure 6. Experimentally determined rotational correlation times τ_C versus molecular mass at 303 K. Each dot corresponds to τ_C and molecular mass of a protein. A solid fitted line represents a regression equation for $\tau_C(x)$ and molecular mass(y), y=2.04x. Dashed lines represent 95% upper and lower prediction confidence limits. The τ_C value of the VAP-A_{MSP}: $OSBP_F$ complex (12.6 ns) and molecular mass of a 1:1 complex (20.2 kDa) are shown by solid vertical and dashed horizontal lines, respectively.

molecular mass of the complex, together with the ITC study, indicates that the complex consists of one VAP-A_{MSP} and one $OSBP_F$.

2.3.3 Structure determination of the complex of VAP-A_{MSP} with $OSBP_F$

The solution structure of the complex of VAP-A_{MSP} with $OSBP_F$ was determined. For structure calculations of the complex, the NOE cross-peaks observed in most NOESY spectra were assigned using the CANDID algorithm of CYANA, while the intermolecular NOE cross-peaks observed in the 3D ^{13}C-edited (F_2)/^{13}C-filtered (F_1) NOESY spectrum were assigned manually. A total of 2825 distance restraints were obtained, and 29 out of 83 intermolecular NOEs were derived from the 3D ^{13}C-edited (F_2)/^{13}C-filtered (F_1) NOESY spectrum (Table 2). The other restraints for structure calculations are shown in Table 2. Using these restraints, structures of the complex were calculated. A superimposed representation of the final 20 lowest energy structures obtained is shown in Figure 7A. The root-mean-square deviations (R.M.S.D.s) of backbone and heavy atoms over residues 6-125 of VAP-A_{MSP} and residues 358-366 of $OSBP_F$ are 0.66 Å and 1.19 Å, respectively (Table 2). Other structural statistics are provided in Table 2.

2.3.4 Global structure

VAP-A_{MSP} has an immunoglobulin-like β-sandwich fold consisting of seven β-strands and one α-helix (Figure 7B). The structure of VAP-A_{MSP} is similar to MSP (Bullock, T.L. *et. al*., 1996; PDB ID, 1MSP), and the positional R.M.S.D. of superimposed C_α atoms is 2.0 Å. The FFAT motif of $OSBP_F$ adopts an extended β-strand-like conformation, and is bent at the C-terminus of the FFAT motif (Figures 7A and B). $OSBP_F$ has an overall negatively charged surface, and binds to VAP-A_{MSP} at a positively charged surface (Figure 7C).

Table 2. Structural statistics for the complex between VAP-A_{MSP} and $OSBP_F$

NOE upper distance restraints	
Intramolecular	
Intraresidual (|i-j| = 0)	691
Sequential (|i-j| = 1)	824
Medium-range (1 < |i-j| < 5)	365
Long-range (≤ |i-j|)	858
Total	2742
Intermolecular	83(29*)
Dihedral angle restraints	
Φ	69
ψ	68
χ_1	13
AMBER GB energies (kcal/ mol)	
Total	-5825 ±6
Constraints	15 ±1
Maximum violations	
Distance (Å)	0.216
Angle (°)	4.868
Mean diviations from ideal geometry	
Bond lengths (Å)	0.0098 ±0.0001
Bond angles (°)	2.29 ±0.02
RMSD (VAP-A 6-125, OSBP 358-366) (Å)	
Backbone atoms	0.66 ±0.14
Heavy atoms	1.19 ±0.16
Ramachandran analysis (VAP-A 6-125, OSBP 358-366) (%)	
Most favored regions	90.6
Additional allowed region	8.1
Generously allowed regions	1.4
Disallowed regions	0.0

* Distance restraints obtained from 3D ^{13}C-edited (F2)/^{13}C-filtered (F1) NOESY

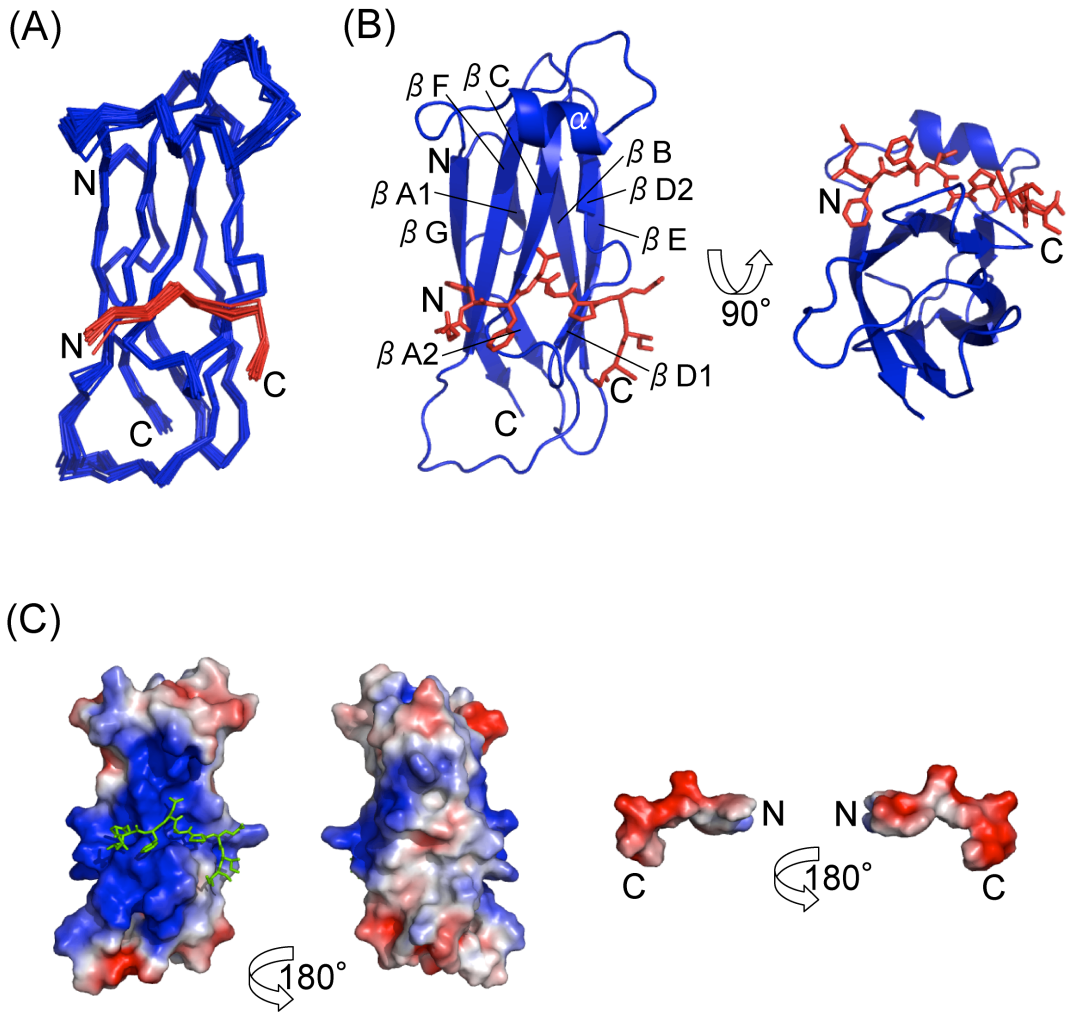

Figure 7. Solution structure of the complex between VAP-A (6-125) and OSBP (358-366). (A) Superimposed representation of 20 lowest energy structures. (B) Ribbon representation of VAP-A_{MSP}. $OSBP_F$ is shown as a stick model. (C) The electrostatic surfaces of VAP-A_{MSP} and $OSBP_F$ contoured from -3 kT (red) to +3 kT (blue). The electrostatic potential was calculated using an AMBER force field.

2.3.5 Interaction between VAP-A_{MSP} and $OSBP_F$

Details of the intermolecular interactions were analyzed using MONSTER (Salerno, W.J. *et. al.*, 2004), and interactions observed in more than 12 structures of the final 20 structures were adopted. The FFAT motif and the C-terminal side of $OSBP_F$ interact with VAP-A_{MSP} β-strands C, D, E, F and a loop connecting β-strands C and D. The complex of VAP-A_{MSP} and $OSBP_F$ is stabilized by electrostatic, hydrophobic and hydrogen bond interactions. Figure 8A shows the interaction site of VAP-A_{MSP} and $OSBP_F$, and Figure 8B shows a schematic representation of the main interactions between $OSBP_F$ and VAP-A_{MSP}. The carboxyl groups of Asp-361 and Glu-364 of $OSBP_F$ interact electrostatically with the side chains of VAP-A_{MSP} Lys-43/Lys-45 and Arg-55, respectively. The proton resonances of VAP-A_{MSP} Lys-43 delta and epsilon positions showed unusual upfield shifts. These shifts may reflect the electrostatic interaction between $OSBP_F$ Asp-361 and VAP-A_{MSP} Lys-43. The side chain of Phe-359 of $OSBP_F$ binds in a hydrophobic pocket formed by residues Lys-45, Thr-47, Lys-87 and Met-89 of VAP-A_{MSP}, and the side chain of Ala-362 of $OSBP_F$ binds in a hydrophobic pocket formed by residues Val-44, Thr-46, Val-54 and Asn-57 of VAP-A_{MSP}. The side chain of Phe-360 of $OSBP_F$ interacts hydrophobically with Pro-49 of VAP-A_{MSP}. The side chains of Pro-363, Glu-364, Ile-365 and Ile-366 of $OSBP_F$ also interact hydrophobically with VAP-A_{MSP}. Three intermolecular backbone-backbone hydrogen bonds are observed between VAP-A_{MSP} and $OSBP_F$, where the amide nitrogens of Thr-46 and Val-54 of VAP-A_{MSP} and Phe-360 of $OSBP_F$ form hydrogen bonds with the carbonyl oxygens of Phe-360 and Pro-362 of $OSBP_F$ and Thr-46 of VAP-A_{MSP} domain, respectively. Amide proton resonances of Thr-46 and Val-54 of VAP-A_{MSP} and Phe-360 of $OSBP_F$ shifted downfield upon complex formation, indicating formation of the respective hydrogen bonds. Intermolecular interactions observed in the structure were further investigated by mutational studies and a series of $OSBP_F$ mutants were generated to achieve this end. For the quantitative

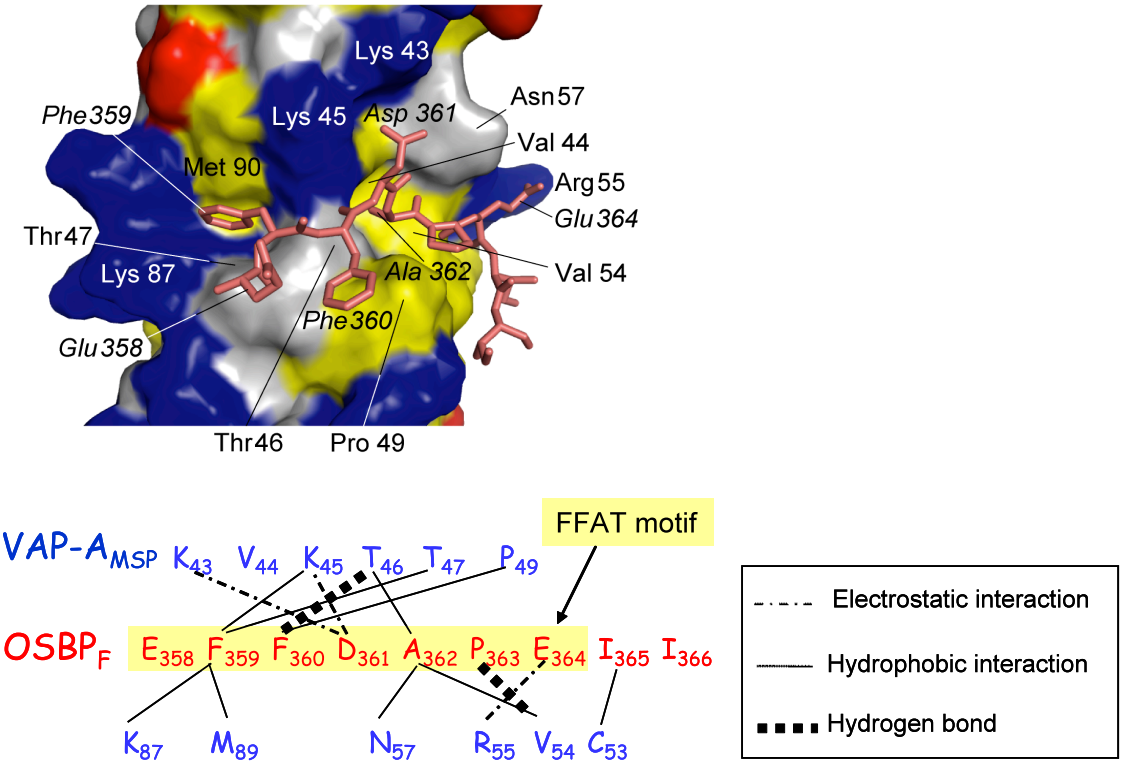

Figure 8. (Top) Details of the interaction. Residue numbers of $OSBP_F$ are written in italics. $OSBP_F$ is shown as a stick model. The surface of VAP-A_{MSP} is represented with acidic (red), basic (blue) and hydrophobic (yellow) residues. (Bottom) A schematic representation of the main interactions between $OSBP_F$ and VAP-A_{MSP}.

Table 3. The dissociation constants (K_d) obtained from the ITC experiments. 10 µl VAP-A_{MSP} (0.9 mM for E356K, 1.2 mM for E364K and 1.0 mM for the others) was titrated into 1.8 ml $OSBP_F$ (63-70 µM) 29 times.

	K_d (M)
E356K	$6.9 \pm 0.7 \times 10^{-6}$
E358A	$4.1 \pm 0.1 \times 10^{-6}$
F360A	$2.1 \pm 0.1 \times 10^{-5}$
F360Q	$1.1 \pm 0.1 \times 10^{-5}$
D361A	$2.8 \pm 0.1 \times 10^{-5}$
E364K	$3.5 \pm 0.3 \times 10^{-5}$
E356K/E364K	$1.1 \pm 0.1 \times 10^{-4}$
WT	$2.1 \pm 0.1 \times 10^{-6}$

analysis, ITC experiments were performed using $OSBP_F$ mutants with VAP-A_{MSP}. The dissociation constants obtained from the ITC experiments are summarized in Table 3. The E356K/E364K double mutant showed the most significant loss of binding to VAP-A_{MSP}. The F360A, D361A and E364K mutants also showed significant loss of binding, while the F360Q mutant showed moderate loss of binding and the E356K and E358A mutants showed only slight loss of binding.

2.3.6 Disorder property of free OSBP

The disorder property of OSBP was examined using the IUPred algorithm (Dosztanyi, Z. *et. al*., 2005, Dosztanyi, Z. *et. al*., 2005). The extensive region of OSBP (Q295-R406), including the FFAT motif (E358-E364), was estimated to be disordered. For experimental investigation of the disordered property of OSBP, ^{1}H-^{15}N hetero NOE was applied to $OSBP_F$. This ^{1}H-^{15}N hetero NOE value is a good indicator of local environment dynamics: negative and large positive NOE values indicate flexible and rigid regions, respectively. All residues of $OSBP_F$ showed negative NOE values in the unbound state (Figure 9A), suggesting that free $OSBP_F$ is flexible. Structure analysis of free $OSBP_F$ using the TALOS program (Cornilescu, G. *et. al*., 1999) with the assigned ^{1}HN, ^{15}N, $^{13}C_{\alpha}$, $^{13}C_{\beta}$ and $^{13}C'$ chemical shifts also showed no ordered structure.

Proteins containing native, unfolded functional regions (> 30-40 residues) under physiological conditions are referred to as intrinsically disordered proteins (IDPs) (Fink, A. L., 2005). A region of more than 100 consecutive residues in OSBP, including 33 residues characterized in this study, seem not to adopt an ordered structure. Thus OSBP may belong to the IDP family.

2.3.7 Changes in dynamics and structure upon complex formation

^{1}H-^{15}N hetero NOE values for the backbone amides of $OSBP_F$ in the bound state are shown in Figure 9A. Upon binding to VAP-A_{MSP}, ^{1}H-^{15}N hetero NOE values of the residues around the FFAT motif of $OSBP_F$ changed from negative to positive, indicating that $OSBP_F$ formed a stable structure upon binding to VAP-A_{MSP}. Figure 9B shows the change in S^2 for the backbone amides of VAP-A_{MSP} upon complex formation. S^2 is a measure of the amplitude of internal motion on the ps~ns time scale, and low (close to 0) and high (close to 1) S^2 values indicate free and restricted motions, respectively. For Tyr-46, Tyr-47 and Arg-51, which are localized at a loop region involved in the binding to $OSBP_F$, S^2 values increased by about 0.35 upon complex formation, indicating that the ps~ns motion of these residues was restricted upon binding to $OSBP_F$ and contributed to formation of a stable complex structure (Figure 10).

Figure 9C shows backbone amide chemical shift changes of $OSBP_F$ and VAP-A_{MSP} upon complex formation. Perturbed residues of $OSBP_F$ were observed for the FFAT motif and the C-terminal side of the FFAT motif, which interact with VAP-A_{MSP} in our structure. Perturbed residues of VAP-A_{MSP} were primarily located within or near the binding site. Two free VAP-A_{MSP} structures have been previously determined (PDB ID; 2CRI (Endo *et. al.*, unpublished) and 1Z9L (Kaiser, S.E. *et. al*., 2005)). Positional R.M.S.D.s of superimposed C_α atoms of our structure with these free VAP-A_{MSP} structures were both 1.3 Å, except for the loop regions (F76-K85). Judging from the chemical shift perturbation and the similarities between our structure and the free structures, the structure of VAP-A_{MSP} does not change markedly upon complex formation.

2.4 Discussion

2.4.1 Comparison with the crystal structure

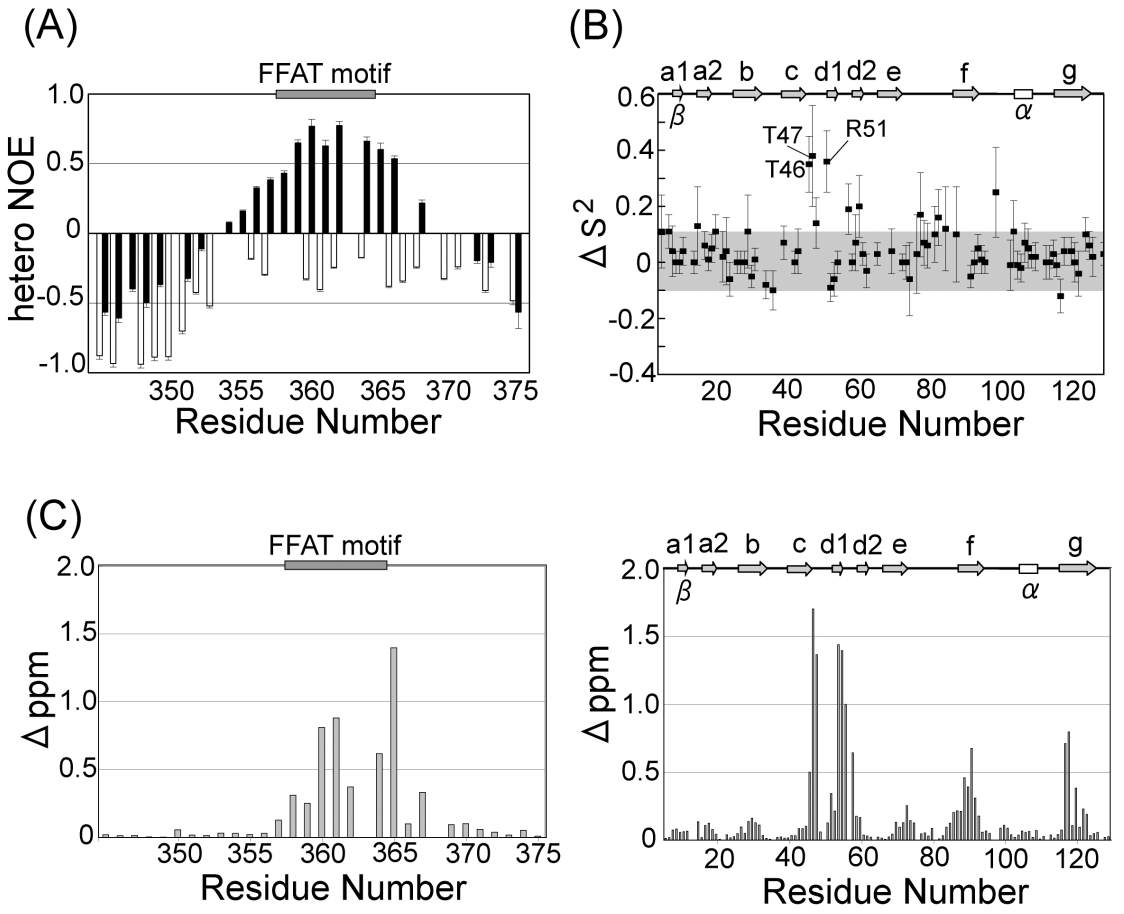

Figure 9. (A) Backbone ^{1}H-^{15}N hetero NOE values of $OSBP_F$ in the unbound (white bar) and bound (black bar) state. Uncertainties were obtained using Monte Carlo simulations. (B) Changes of S^2 values of VAP-A_{MSP} upon complex formation with $OSBP_F$. ΔS^2 = S^2 (complex) - S^2 (free). The region between ΔS^2 = -0.1 ~ 0.1 is shadowed. (C) Composite chemical shift changes of VAP-A_{MSP} and $OSBP_F$ upon complex formation. Composite chemical shift changes were calculated using the equation $\Delta ppm = \{(\Delta\delta_H)^2 + (\Delta\delta_N/5)^2\}^{1/2}$, where $\Delta\delta_H$ and $\Delta\delta_N$ represent the chemical shift changes of ^{1}H and ^{15}N, respectively.

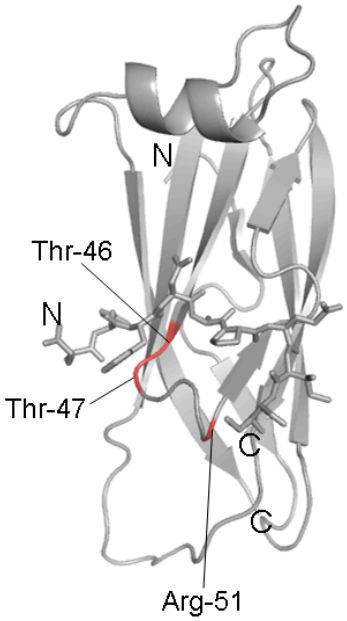

Figure 10. Residues showing increased S^2 values about 0.35 upon complex formation.

A crystal structure of a complex between rat VAP-A_{MSP} and rat ORP1 fragment containingthe FFAT motif (SEDEFYDALS) ($ORP1_F$) has been determined (Kaiser, S.E. *et. al*., 2005). The overall structures of our structure and the crystal structure (PDB ID; 1Z9O) are similar (Figure 11A), and the positional R.S.M.D. of superimposed C_α atoms of VAP-A_{MSP} and the FFAT motif are 1.2 Å, although the crystal structure is composed of two VAP-A_{MSP} and two $ORP1_F$ molecules. Clear differences were observed for the intermolecular interactions in that side chains of the 3rd Phe/Tyr and 4th Asp residues of the FFAT motif (the consensus sequence "EFFDAxE") interact with VAP-A_{MSP} in the solution structure. In the crystal structure, these residues do not interact with VAP-A_{MSP} but interact with the second $ORP1_F$ molecule to stabilize the 2:2 complex (Kaiser, S.E. *et. al*., 2005) (Figure 11B). Substitution of the 4th Asp of the FFAT motif with Ala disrupts ER localization of Osh1, a yeast protein containing the FFAT motif (Loewen, C.J. *et. al*., 2003), and disrupts the interaction of CERT, a ceramide transport protein containing the FFAT motif, with VAP-A *in vivo* (Kawano, M. *et. al.*, 2006). These results are consistent with our solution structure since the side chain of the 4th Asp residue of the FFAT motif interacts directly with VAP-A_{MSP}. Thus, we assume that formation of the solution structure, comprising a 1:1 complex between VAP-A_{MSP} and a FFAT protein, is essential for binding of the FFAT protein to VAP-A.

2.4.1 Recognition mechanism of intrinsically disordered $OSBP_F$ by VAP-A_{MSP}

In an effort to further understand the recognition mechanism of $OSBP_F$ by VAP-A_{MSP}, we inspected the perturbed chemical shift patterns in titration experiments that were carried out using ^{15}N-labeled VAP-A_{MSP} or $OSBP_F$. Nonlinear behavior was found for 8 residues of VAP-A_{MSP}, whereas the other peaks show fast/intermediate lineshapes with linear patterns (Figure 12A). NMR lineshapes reflect the relationship between the frequency difference ($\Delta\nu$) of two states and the exchange rate (k_{ex}). To determine whether the nonlinear patterns

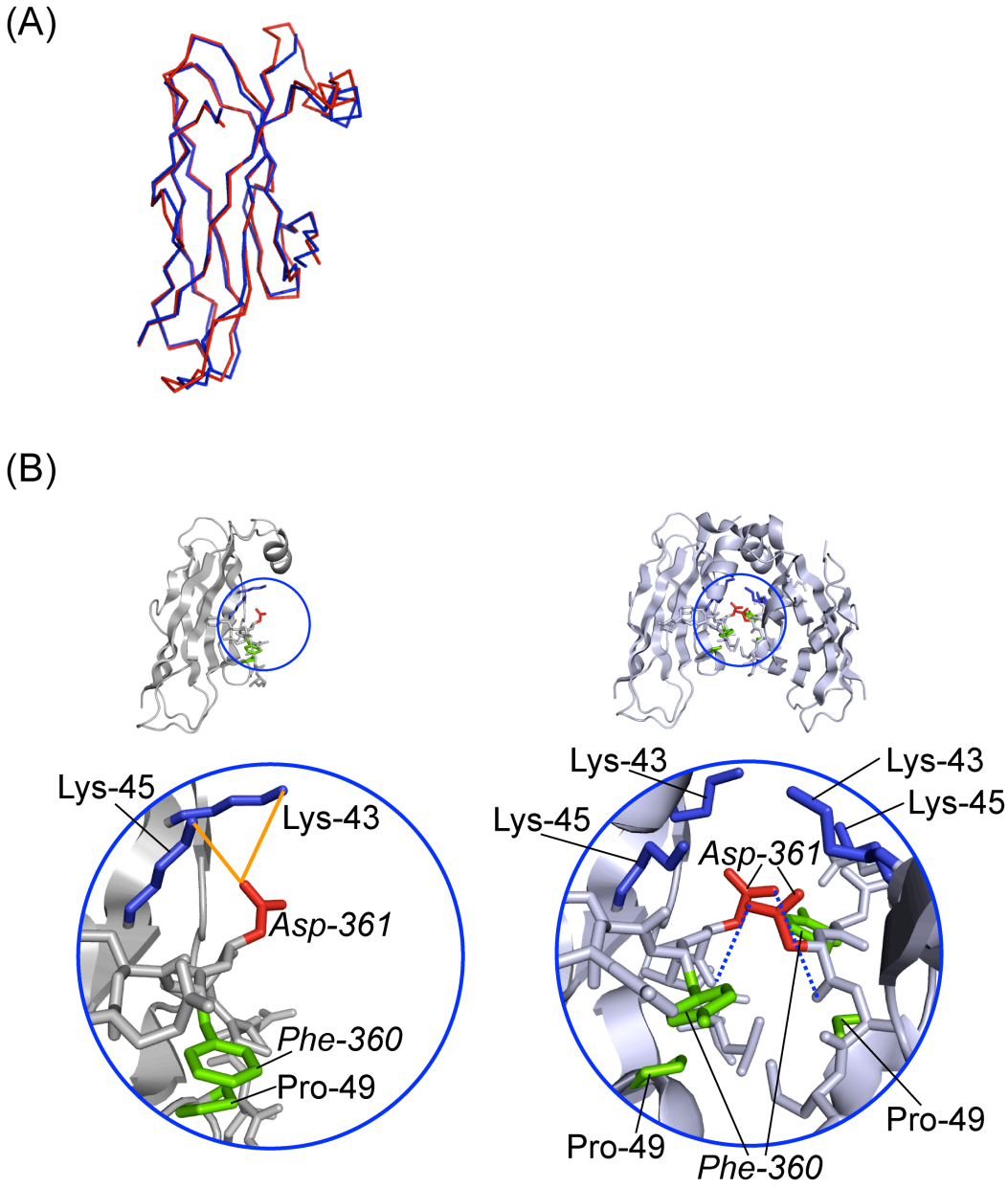

Figure 11. (A) Superimposed picture of the solution structure (red) and the crystal structure (blue) of the complex. (B) Comparison of intermolecular interaction between the solution structure (left) and the crystal structure (right). Electrostatic interactions are shown by orange lines. Hydrogen bonds are shown by blue dotted lines. Residue numbers of $OSBP_F$ are written in italics.

observed could be reproduced with a two-site model, we simulated titration curves with various k_{off} values under conditions satisfying the experimentally determined K_d value and input concentrations of VAP-A_{MSP} and $OSBP_F$ using the LineShapeKin software package. The simulation could only account for the behavior of 4 residues, while the other 4 residues, Ser-58, Gln-74, Gln-91 and Cys-121, remained elusive using the two-site exchange model (Figure 12A and 12B). The complicated features of these residues were revealed by inspecting the lineshapes of these residues. For instance, Cys-121 consisted of 4 peaks at a 1:0.44 molar ratio of VAP-A_{MSP} to $OSBP_F$ as shown in Figure 13A. The overlaid 1D titration curve of Gln-91 also displayed 3 peak tops at a molar ratio of 1:0.59 (Figure 13B). Glu-74 showed two peaks at a molar ratio of 1:0.59 (Figure 13C). One is found at 8.03 ppm ^1H between free (8.13 ppm) and complex (7.99 ppm) peak positions, and the other (8.14 ppm) is out of range. A convincing explanation for these observations is to assume formation of intermediate states. The intermediate complex is thought to be maintained by non-specific interactions, considering the observations that the peaks in the middle of the titration have several peak tops.

We hypothesized that electrostatic interactions between $OSBP_F$ and VAP-A_{MSP} play a role in forming the intermediate, since initial screening of sample conditions showed that the titration under 500 mM KCl does not reach saturation even at a 10:1 ratio of $OSBP_F$ to VAP-A_{MSP} (data not shown). Additionally, VAP-A_{MSP} has a large basic area at the same surface in the region which $OSBP_F$ binds to (Figure 7C), and a plethora of acidic residues are found in $OSBP_F$ as well as its homologous sequences. In addition to the three acidic residues that are within the FFAT motif, there is an acidic patch of 5 residues comprising Asp-352, Glu-353, Asp-354, Asp-355 and Glu-356 at a region preceding the FFAT motif. This acidic patch region does not converge in the final ensemble structures due to the lack of medium- to long-range intra- and inter-molecular NOE restraints, suggesting that there is no stable

(A)

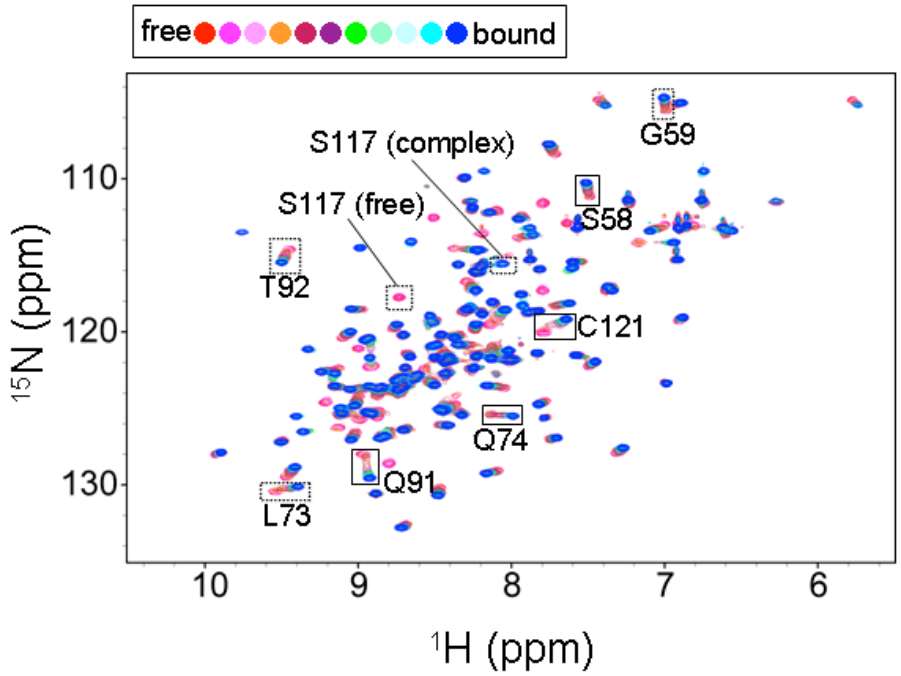

(B)

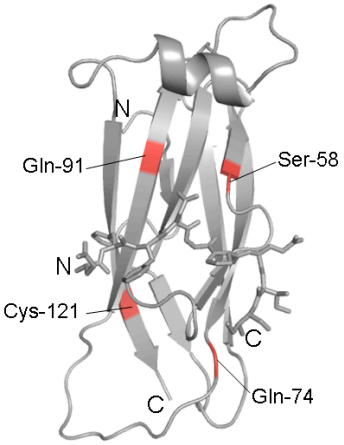

Figure 12. (A) An overlay of ^{1}H-^{15}N HSQC spectra obtained during titration of VAP-A_{MSP} with $OSBP_F$. Concentration ratios (VAP-A_{MSP}:$OSBP_F$) ranged from 1:0 (red) to 1:1.76 (blue). Cross-peaks for residues for which peak shifts are not explained by a two-site exchange model are shown in solid rectangles. Cross-peaks for residues for which peak shifts are nonlinear but explained by a two-site exchange model are shown in dashed rectangles. (B) The localizations of residues for which peak shifts are not explained by a two-site exchange model.

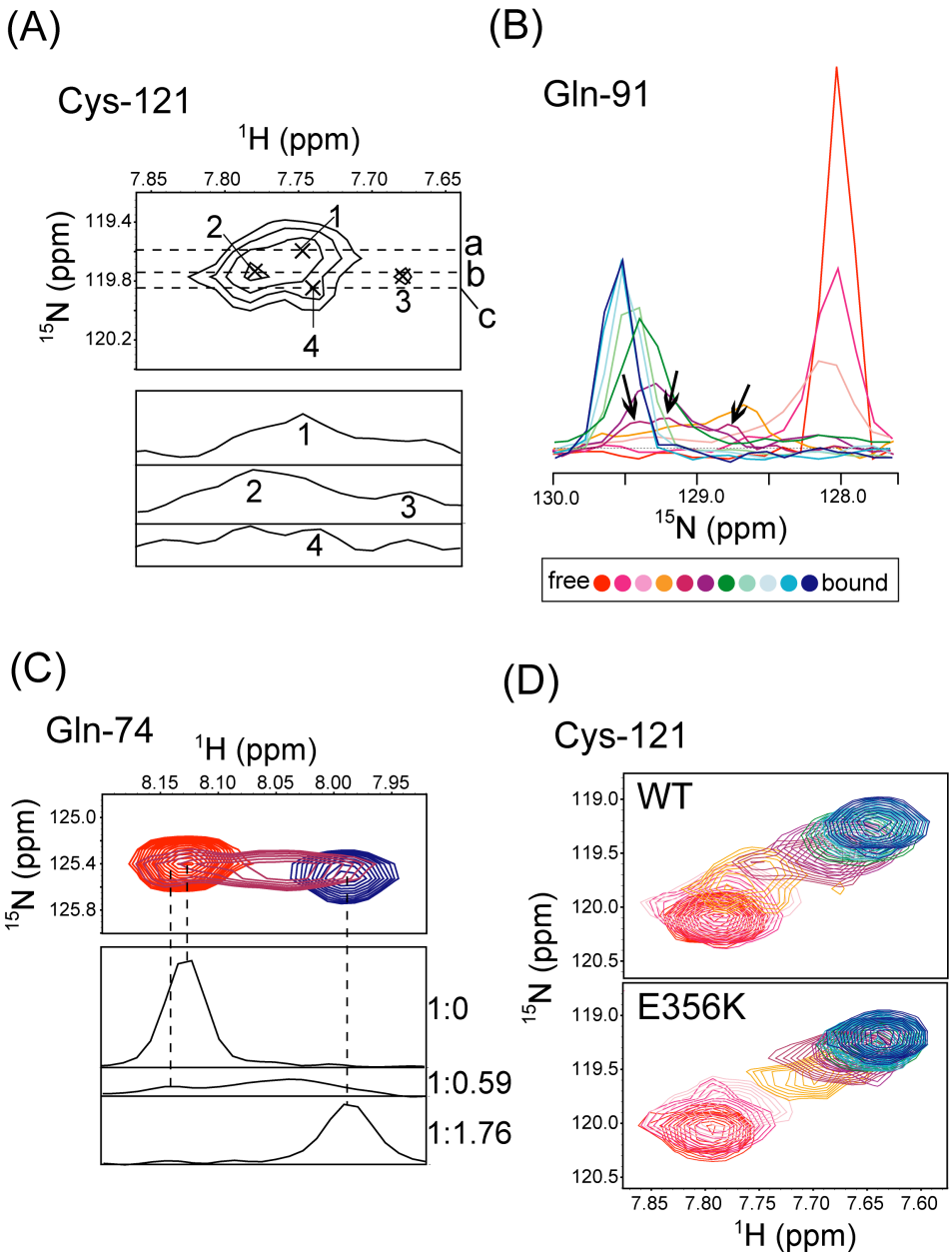

Figure 13. (A) Cross-peaks of Cys-121 at a molar ratio of $OSBP_F$ to VAP-A_{MSP} of 1:0.44. In the upper figure, peaks are indicated by a cross and are labeled. The lower figure shows ^{1}H cross-sections corresponding to lines a, b and c in the upper figure. Numbers indicate corresponding peaks in the upper figure. (B) An overlay of ^{15}N cross-sections of Gln-91 in a titration of VAP-A_{MSP} with $OSBP_F$. Molar ratios (VAP-A_{MSP}:$OSBP_F$) ranged from 1:0 (red) to 1:1.76 (blue). Peak tops at a molar ratio of 1:0.59 are shown by arrows. (C) The upper figure shows an overlay of cross-peaks for Gln-74 at molar ratios of $OSBP_F$ of 0 (red), 0.59 (purple) and 1.76 (blue). The lower figure shows ^{1}H cross-sections of peaks at each molar ratio. Corresponding peaks in the upper and lower figures are connected by dashed lines. (D) Comparison of cross-peaks for Cys-121 in titrations with $OSBP_F$ (WT) and the E356K mutant.

interaction between the acidic patch and VAP-A_{MSP}. This is also indicated by small difference in chemical shifts before and after binding to VAP-A_{MSP} and the lower hetero NOE values of these residues in the complex (Figures 9A and B). We examined the role of the acidic patch by preparing the charge reversal E356K mutant of $OSBP_F$ and conducting titration experiments using ^{15}N-labeled VAP-A_{MSP}. Remarkably in this case, with the exception of Gln-74 and Gln-91, the nonlinear patterns that were found in titrations with WT disappeared, thereby allowing for simulation using a two-site model (Figure 13D). It should be noted that the chemical shifts of VAP-A_{MSP} in the saturated state are similar even in the complex with the E356K mutant, implying that the final structures are similar. Nonetheless, the ITC experiment showed that the E356K mutant has reduced binding affinity for VAP-A_{MSP} (Table 3). In a three-site exchange consisting of free, intermediate and binding complex, the exchange between the intermediate and final product is expected to be much faster than that between the free and intermediate states. The E356K mutant probably possesses an increased off-rate from the intermediate to free conformation, which in turn leads to higher values of K_d and a faster apparent exchange rate. These results suggest the possibility that the acidic patch of $OSBP_F$ including Glu-356 of $OSBP_F$ takes part in increasing the apparent binding affinity by contributing to the formation of an intermediate complex with VAP-A_{MSP} through electrostatic interactions. Thus it is reasonable to assume that OSBP recognizes VAP-A through "coupled folding and binding" process. However, we do not have any data to deny the existence of pre-equilibrated bound conformer of $OSBP_F$ in the unbound state, and cannot exclude the "conformation selection" model.

2.4.3 Effects of P56S mutation on VAP_{MSP}

The P56S mutation in human VAP-B causes familial autosomal dominant motoneuronal diseases, ALS8, which exhibits a typical ALS phenotype with rapid

progression or late onset spinal muscular atrophy (Nishimura, A.L., *et. al*., 2004). The P56S mutation in VAP-B induces insolubility and aggregate formation of VAP-B (Kanekura, K. *et. al.*, 2006). Pro-56 is conserved not only in the VAP family of proteins but also in the MSP family of proteins (Tarr, D.E. *et. al.*, 2005). In order to investigate the effects of the P56S mutation on VAP_{MSP}, we prepared the P56S mutant of VAP-A_{MSP}. Figure 13A shows the ^{1}H-^{15}N HSQC spectrum of P56S VAP-A_{MSP} superimposed on that of WT VAP-A_{MSP}. The number of peaks in the ^{1}H-^{15}N HSQC spectrum of P56S VAP-A_{MSP} was greater than that expected from the amino acid sequence of P56S VAP-A_{MSP}. Some residues of P56S VAP-A_{MSP} probably gave double peaks and the intensities of these double peaks were similar. Hence, it is concluded that P56S VAP-A_{MSP} has two conformations with similar abundance.

We then investigated the ability of P56S VAP-A_{MSP} to bind the FFAT motif. Figure 13B shows the ^{1}H-^{15}N HSQC spectrum of P56S VAP-A_{MSP} in the presence of $OSBP_F$ superimposed on that in the absence of $OSBP_F$. Both double peaks were perturbed by the addition of $OSBP_F$. Therefore, both conformations of P56S VAP-A_{MSP} can bind to $OSBP_F$. In the presence of $OSBP_F$, some double peaks have similar intensity (Figure 14B, upper box), while others have different intensities (Figure 14B, lower box). It seems that the binding modes for $OSBP_F$ differ between the two conformations.

We then investigated the thermodynamic stability of P56S VAP-A_{MSP} by DSC (Figure 14C). The temperature of maximum heat capacity of WT VAP-A_{MSP} is 64.6 ºC and that of P56S VAP-A_{MSP} is 49.0 ºC, indicating that P56S VAP-A_{MSP} is thermally unstable. The heat capacity peak of P56S VAP-A_{MSP} is broader than that of WT, indicating that the change in enthalpy (ΔH) of protein unfolding of P56S VAP-A_{MSP} is smaller than that of WT. In fact, DSC curve analyses showed that ΔH of protein unfolding of WT and P56S VAP-AMSP are 529 and 416 (43.6 at 64.6 ºC) kJ/mol, respectively. The decrease in ΔH of protein unfolding associated with the P56S mutation indicates that the thermal instability of P56S VAP-A_{MSP}

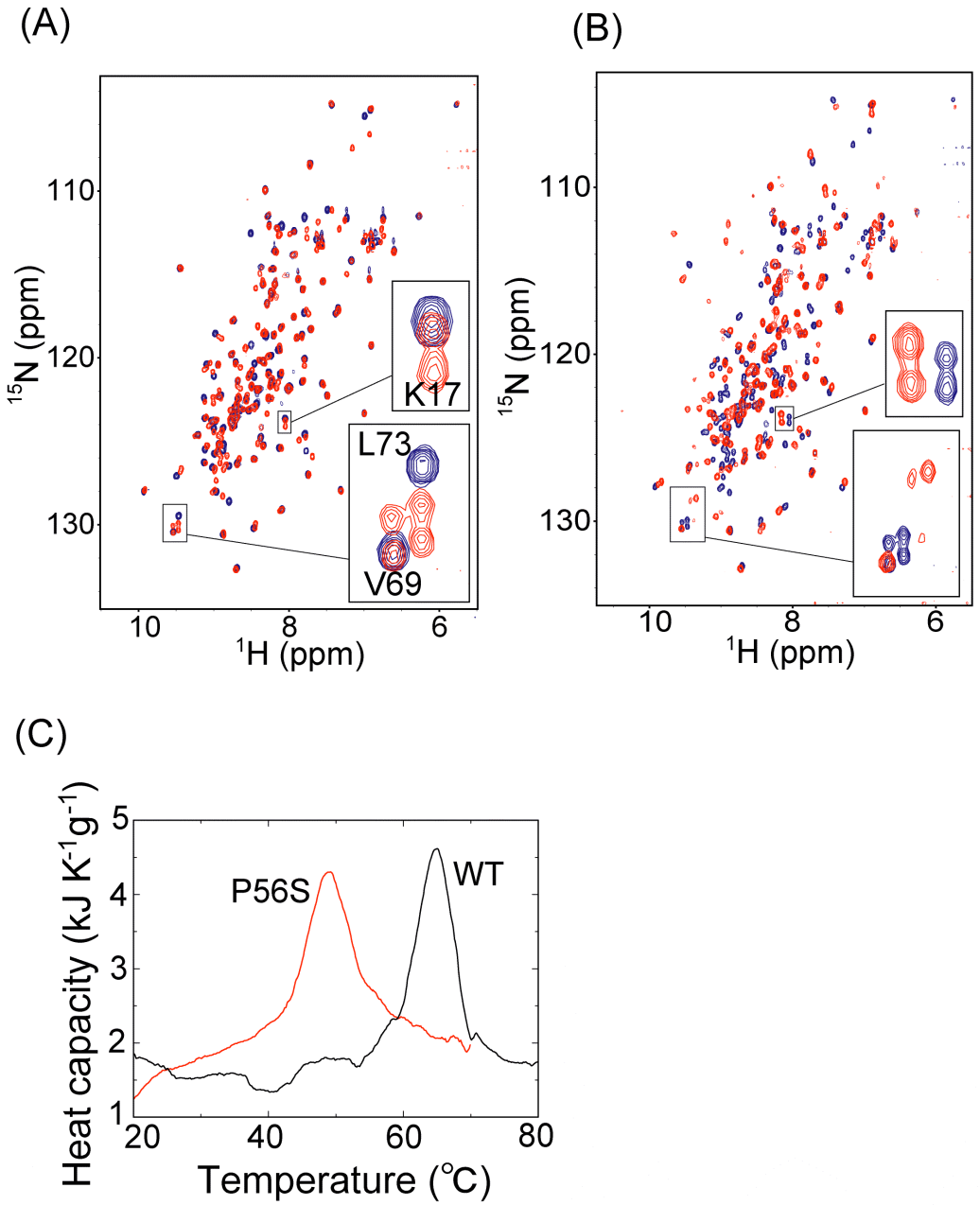

Figure 14. (A) ^{1}H-^{15}N HSQC spectra of P56S (red) and WT (blue) VAP-A_{MSP}. In the boxed region, assignments of peaks of WT VAP-A_{MSP} are indicated. (B) ^{1}H-^{15}N HSQC spectra of P56S VAP-A_{MSP} in the presence of $OSBP_F$ with a molar ratio of 1:2 (red) and in the absence of $OSBP_F$ (blue). (C) DSC profiles of P56S (red) and WT (black) VAP-A_{MSP}.

results from losses of hydrogen bonds and/or *van der Waals* interactions in the protein. As judged by the ^{1}H-^{15}N HSQC spectra of P56S and WT VAP-A_{MSP}, the structure of P56S VAP-A_{MSP} does not differ greatly from that of WT. However, results of the DSC experiments showed that P56S VAP-A_{MSP} is more thermally unstable than WT. Since the MSP domains of VAP-A and VAP-B share 82% amino acid sequence identity, their structures are probably similar. It is likely that the effects of the P56S mutation on VAP-B_{MSP} are similar to the effects of the P56S mutation on VAP-A_{MSP}. Thus, it is reasonable to assume that the P56S mutation in VAP-B decreases the thermal stability of VAP-B, and facilitates aggregation.

2.5 Conclusion

In this study, we have determined the solution structure of the complex between VAP-A_{MSP} and $OSBP_F$ and found that all residues in the FFAT motif except for Glu-358 interact with VAP-A_{MSP}. Furthermore, NMR titration and relaxation, ITC and mutagenesis studies suggest that $OSBP_F$ is disordered in the unbound state and VAP-A_{MSP} and $OSBP_F$ form a final complex by means of intermediates involving acid patch preceding the FFAT motif (Figure 15).

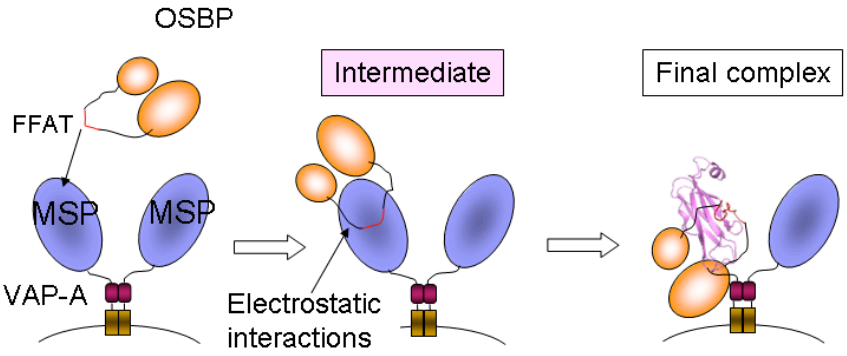

Figure 15. The recognition mechanism of the disordered region of OSBP by VAP-A_{MSP}.

3. **General conclusion**

In this thesis, we have studied molecular recognition mechanisms using NMR spectroscopy. In the main part of this thesis, we have studied the interaction between VAP-A_{MSP} and $OSBP_F$. We determined the solution structure of the complex between VAP-A_{MSP} and $OSBP_F$, and identified important interactions for their binding (Figures 7 and 8). In our structure, all residues except for Glu-358 of FFAT motif interact with VAP-A_{MSP}. NMR relaxation experiments showed that free $OSBP_F$ is disordered, but the structure is stabilized by the binding to VAP-A_{MSP} (Figure 9A). NMR titration experiments showed that VAP-A_{MSP} and $OSBP_F$ form intermediate complex before forming stable complex (Figure 12 and 13). No interaction between acidic residues at the N-terminal side of the FFAT motif and VAP-A_{MSP} was detected in our structure. However, one of these acidic residues (Glu-356) was involved in the formation of the intermediate complex (Figure 13) and the E356K mutation reduced the binding affinity for VAP-A_{MSP} by about 3-fold (Table 3). These results are consistent with "coupled binding and folding" model. In this model, it has been hypothesized on theoretical grounds that the binding kinetics is enhanced by a "fly-casting" effect, briefly the disordered protein binds weakly and non-specifically to its target followed by the folding, where the protein approaches the binding site (Shoemaker,B.A. *et. al*., 2000). Our results suggest that $OSBP_F$ initially bind VAP-A_{MSP} through non-specific charge interactions involving acidic residues at the N-terminal side of the FFAT motif and finally forms a stable complex structure through a "fly-casting"-like process.

In Appendix, we have performed solution NMR studies of two DNA oligomers, which contain cyclic 2'-deoxyuridylate dimmers connected by ethylene (U^{et}_pU) or propylene (U^{pr}_pU) linkages. Our NMR titration experiments and previous report indicated that the U^{et}_pU DNA oligomer has higher affinity for HMGB1 A-box than the U^{pr}_pU DNA oligomer (Appendix

Figure 11; Murata, S. *et. al.*, 2007). We determined solution structures of these DNA oligomers (Appendix Figure 7), which revealed that local structure around cross-linked site of the $U^{et}_{p}U$ DNA oligomer is similar to that of cisplatin linked DNA oligomer complexed with HMGB1 A-box (Ohndorf, U.M. *et. al.*, 1999), whereas that of the $U^{pr}_{p}U$ DNA oligomer is not (Appendix Table 2; Appendix Figure 9). Therefore we concluded that the free DNA structure similar to the bound conformation is important for the strong binding to HMGB1 A-box, and the DNA recognition mechanism of HMGB1 A-box is explained by "lock and key" mechanism.

Our studies showed that the disordered region of OSBP and HMGB1 A-box recognize their binding targets through quite different mechanisms, "coupled binding and folding" and "lock and key" mechanisms, respectively (Figure 15 and Appendix Figure 15). Respective molecular recognition mechanisms may be related to their biological roles. Scaffolding proteins are known to often use short peptide motifs within large intrinsically disordered segments in order to anchor proteins to specific sub-cellular localizations (Gsponer, J. and Babu, M.M., 2009), where the flexible nature of IDPs is supposed to permit the peptide motifs to easily access the binding targets, and facilitate their bindings through "fly-casting" mechanism. Similarly, OSBP will make use of the intrinsically disordered region containing FFAT motif in order to be localized at the ER by interaction with VAP-A. OSBP is supposed to change the conformation upon binding of the lipid ligands (Lehto, M. *et. al*., 2003; Im, Y.J., *et. al*., 2005) (Figure 2), which requires flexible segment between the PH and LB domains (Figure 1). Thus it is reasonable to assume that OSBP uses the "coupled binding and folding" mechanism in order to be localized at the ER while it keeps the high flexibility of the central region. On the other hand, the "lock and key" mechanism is supposed to provide highly specific binding. HMGB1 is a structure-specific DNA binding protein. However, HMGB1 A-box binds any DNA by non-specific charge interactions (Appendix Figure 12). Therefore it

may select “lock and key” mechanism in order to gain high specificity for its target DNAs.

4. Acknowledgements

The present study has been performed under the direction of Dr. Chojiro Kojima (Graduate School of Biological Sciences, Nara Institute of Science and Technology). I would like to express my great appreciation to him for his guidance and discussions throughout this study.

I wish to thank Drs. JunGoo Jee (Center for Priority Areas, Tokyo Metropolitan University) and Masaki Mishima (Graduate School of Science and Engineering, Tokyo Metropolitan University) for teaching me experimental techniques and helpful discussions.

I wish to thank Dr. Harumi Fukada (Graduate School of Life and Environmental Sciences, Osaka Prefecture University) for ITC measurements and precious discussions.

I wish to thank Drs. Shunpei Murata, Satoshi Ichikawa and Akira Matsuda (Faculty of Pharmaceutical Sciences, Hokkaido University) for the gifts of DNA oligomer samples.

I wish to thank to Ms Momoko Yoneyama and Ms Hiroko Kinoshita (Graduate School of Biological Sciences, Nara Institute of Science and Technology) for their excellent technical assistance.

I would like to thank to Dr. Toshio Hakoshima, and all the members of his group and Dr. Chojiro Kojima's group (Graduate School of Biological Sciences, Nara Institute of Science and Technology) for their kindness. I could carry out my experiments comfortably.

Finally I would like to thank my family for their supports and understanding.

Kyoko Furuita

January 25, 2010

5. References

Amarilio, R., Ramachandran, S., Sabanay, H., and Lev, S. (2005). Differential regulation of endoplasmic reticulum structure through VAP-Nir protein interaction. J. Biol. Chem. *280,* 5934-5944.

Archer, S.J., Ikura, M., Torchia, D.A., and Bax, A. (1991). An Alternative 3D NMR Technique for Correlating Backbone ^{15}N with Side Chain ^{1}H Resonances in Larger Proteins. J. Magn. Reson. *91,* 636-641.

Bianchi, M.E. (1988). Interaction of a protein from rat liver nuclei with cruciform DNA. EMBO J. *7,* 843-849.

Bianchi, M.E., Beltrame, M., and Paonessa, G. (1989). Specific recognition of cruciform DNA by nuclear protein HMG1. Science *243,* 1056-1059.

Bodenhausen, G., and Ruben, D.J. (1980). Natural abundance nitrogen-15 NMR by enhanced heteronuclear spectroscopy. Chem. Phys. Lett *69,* 185-189.

Borgias, B.A., and James, T.L. (1989). Two-dimensional nuclear Overhauser effect: complete relaxation matrix analysis. Methods Enzymol. *176,* 169-183.

Braunschweiler, L., and Ernst, R.R. (1983). Coherence transfer by isotropic mixing: Application to proton correlation spectroscopy. J. Magn. Reson. *53,* 521-528.

Brickner, J.H., and Walter, P. (2004). Gene recruitment of the activated INO1 locus to the nuclear membrane. PLoS Biol. *2,* e342.

Brunger, A.T. (2007). Version 1.2 of the Crystallography and NMR system. Nat. Protoc. *2,* 2728-2733.

Brunger, A.T., Adams, P.D., Clore, G.M., DeLano, W.L., Gros, P., Grosse-Kunstleve, R.W., Jiang, J.S., Kuszewski, J., Nilges, M., Pannu, N.S.*, et al.* (1998). Crystallography & NMR system: A new software suite for macromolecular structure determination. Acta Crystallogr. D Biol. Crystallogr. *54,* 905-921.

Bullock, T.L., Roberts, T.M., and Stewart, M. (1996). 2.5 A resolution crystal structure of the motile major sperm protein (MSP) of Ascaris suum. J. Mol. Biol. *263,* 284-296.

Catez, F., Yang, H., Tracey, K.J., Reeves, R., Misteli, T., and Bustin, M. (2004). Network of dynamic interactions between histone H1 and high-mobility-group proteins in chromatin. Mol. Cell. Biol. *24,* 4321-4328.

Cavanagh, J., Fairbrother, W. J., Palmer, A. G., Rance, M. and Skelton, N. J. (2007) Protein NMR spectroscopy (2^{nd} edition), Academic Press, San Diego.

Cornilescu, G., Delaglio, F., and Bax, A. (1999). Protein backbone angle restraints from searching a database for chemical shift and sequence homology. J. Biomol. NMR *13,* 289-302.

Das, D., and Scovell, W.M. (2001). The binding interaction of HMG-1 with the TATA-binding protein/TATA complex. J. Biol. Chem. *276,* 32597-32605.

Delaglio, F., Grzesiek, S., Vuister, G.W., Zhu, G., Pfeifer, J., and Bax, A. (1995). NMRPipe: a multidimensional spectral processing system based on UNIX pipes. J. Biomol. NMR *6,* 277-293.

Dosset, P., Hus, J.C., Blackledge, M., and Marion, D. (2000). Efficient analysis of macromolecular rotational diffusion from heteronuclear relaxation data. J. Biomol. NMR *16,* 23-28.

Dosztanyi, Z., Csizmok, V., Tompa, P., and Simon, I. (2005). IUPred: web server for the prediction of intrinsically unstructured regions of proteins based on estimated energy content. Bioinformatics *21,* 3433-3434.

Dosztanyi, Z., Csizmok, V., Tompa, P., and Simon, I. (2005). The pairwise energy content estimated from amino acid composition discriminates between folded and intrinsically unstructured proteins. J. Mol. Biol. *347,* 827-839.

Endo, H., Hayashi, F., Yoshida, M., Yokoyama, S., Solution structure of the MSP domain of mouse VAMP-associated proteinA, unpublished.

Espinoza-Fonseca, L.M. (2009). Reconciling binding mechanisms of intrinsically disordered proteins. Biochem. Biophys. Res. Commun. *382,* 479-482.

Fink, A.L. (2005). Natively unfolded proteins. Curr. Opin. Struct. Biol. *15,* 35-41.

Fischer, E. (1894). Einfluss der configuration auf die Wirkung der Enzyme. Ber. Dtsch. Chem. Ges. *27*, 2985–2991.

Foster, L.J., Weir, M.L., Lim, D.Y., Liu, Z., Trimble, W.S., and Klip, A. (2000). A functional role for VAP-33 in insulin-stimulated GLUT4 traffic. Traffic *1,* 512-521.

Gao, L., Aizaki, H., He, J.W., and Lai, M.M. (2004). Interactions between viral nonstructural proteins and host protein hVAP-33 mediate the formation of hepatitis C virus RNA replication complex on lipid raft. J. Virol. *78,* 3480-3488.

Garvie, C.W., and Wolberger, C. (2001). Recognition of specific DNA sequences. Mol. Cell *8,* 937-946.

Garza, A.S., Ahmad, N., and Kumar, R. (2009). Role of intrinsically disordered protein regions/domains in transcriptional regulation. Life Sci. *84,* 189-193.

Goda, N., Tenno, T., Takasu, H., Hiroaki, H., and Shirakawa, M. (2004). The PRESAT-vector: asymmetric T-vector for high-throughput screening of soluble protein domains for structural proteomics. Protein Sci. *13,* 652-658.

Grzesiek, S., Ikura, M., Clore, G.M., Gronenborn, A.M., and Bax, A. (1992). A 3D Triple-Resonance Technique for Qualitative Measurement of Carbonyl-H J Couplings in Isotopically Enriched Proteins. J. Magn. Reson. *95,* 636-641.

Gsponer, J., and Babu, M.M. (2009). The rules of disorder or why disorder rules. Prog. Biophys. Mol. Biol. *99,* 94-103.

Guntert, P. (2004). Automated NMR structure calculation with CYANA. Methods Mol. Biol. *278,* 353-378.

Guntert, P., Mumenthaler, C., and Wuthrich, K. (1997). Torsion angle dynamics for NMR structure calculation with the new program DYANA. J. Mol. Biol. *273,* 283-298.

Hardman, C.H., Broadhurst, R.W., Raine, A.R., Grasser, K.D., Thomas, J.O., and Laue, E.D. (1995). Structure of the A-domain of HMG1 and its interaction with DNA as studied by heteronuclear three- and four-dimensional NMR spectroscopy. Biochemistry *34,* 16596-16607.

Herrmann, T., Guntert, P., and Wuthrich, K. (2002). Protein NMR structure determination with automated NOE assignment using the new software CANDID and the torsion angle dynamics algorithm DYANA. J. Mol. Biol. *319,* 209-227.

Hu, J.S., and Bax, A. (1997). Chi 1 angle information from a simple two-dimensional NMR experiment that identifies trans $^{3}J_{NC}$ gamma couplings in isotopically enriched proteins. J. Biomol. NMR *9,* 323-328.

Hu J. S., and Bax, A. (1997). Determination of and Chi 1 Angles in Proteins from ^{13}C-^{13}C Three-Bond *J* Couplings Measured by Three-Dimensional Heteronuclear NMR. How Planar Is the Peptide Bond? J. Am. Chem. Soc *119,* 6360-6368.

Hughes, E.N., Engelsberg, B.N., and Billings, P.C. (1992). Purification of nuclear proteins that bind to cisplatin-damaged DNA. Identity with high mobility group proteins 1 and 2. J. Biol. Chem. *267,* 13520-13527.

Im, Y.J., Raychaudhuri, S., Prinz, W.A., and Hurley, J.H. (2005). Structural mechanism for sterol sensing and transport by OSBP-related proteins. Nature *437,* 154-158.

Jaworski, C.J., Moreira, E., Li, A., Lee, R., and Rodriguez, I.R. (2001). A family of 12 human genes containing oxysterol-binding domains. Genomics *78,* 185-196.

Kaiser, S.E., Brickner, J.H., Reilein, A.R., Fenn, T.D., Walter, P., and Brunger, A.T. (2005). Structural basis of FFAT motif-mediated ER targeting. Structure *13,* 1035-1045.

Kanekura, K., Nishimoto, I., Aiso, S., and Matsuoka, M. (2006). Characterization of amyotrophic lateral sclerosis-linked P56S mutation of vesicle-associated membrane protein-associated protein B (VAPB/ALS8). J. Biol. Chem. *281,* 30223-30233.

Kawano, M., Kumagai, K., Nishijima, M., and Hanada, K. (2006). Efficient trafficking of ceramide from the endoplasmic reticulum to the Golgi apparatus requires a VAMP-associated protein-interacting FFAT motif of CERT. J. Biol. Chem. *281,* 30279-30288.

Klune, J.R., Dhupar, R., Cardinal, J., Billiar, T.R., and Tsung, A. (2008). HMGB1: endogenous danger signaling. Mol. Med. *14,* 476-484.

Koshland, D. E. J. (1958). Application of a theory of enzyme specificity to protein synthesis. Proc. Natl Acad. Sci. USA *44*, 98–123.

Kovrigin, E.L., and Loria, J.P. (2006). Enzyme dynamics along the reaction coordinate: critical role of a conserved residue. Biochemistry *45,* 2636-2647.

Lapierre, L.A., Tuma, P.L., Navarre, J., Goldenring, J.R., and Anderson, J.M. (1999). VAP-33 localizes to both an intracellular vesicle population and with occludin at the tight junction. J. Cell. Sci. *112 (Pt 21),* 3723-3732.

Laskowski, R.A., Rullmannn, J.A., MacArthur, M.W., Kaptein, R., and Thornton, J.M. (1996). AQUA and PROCHECK-NMR: programs for checking the quality of protein structures solved by NMR. J. Biomol. NMR *8,* 477-486.

Lavery, R., and Sklenar, H. (1989). Defining the structure of irregular nucleic acids: conventions and principles. J. Biomol. Struct. Dyn. *6,* 655-667.

Lehto, M., Laitinen, S., Chinetti, G., Johansson, M., Ehnholm, C., Staels, B., Ikonen, E., and Olkkonen, V.M. (2001). The OSBP-related protein family in humans. J. Lipid Res. *42,* 1203-1213.

Lehto, M., and Olkkonen, V.M. (2003). The OSBP-related proteins: a novel protein family involved in vesicle transport, cellular lipid metabolism, and cell signalling. Biochim. Biophys. Acta *1631,* 1-11.

Lehto, M., Tienari, J., Lehtonen, S., Lehtonen, E., and Olkkonen, V.M. (2004). Subfamily III of mammalian oxysterol-binding protein (OSBP) homologues: the expression and intracellular localization of ORP3, ORP6, and ORP7. Cell Tissue Res. *315,* 39-57.

Liu, H., Spielmann, H.P., Ulyanov, N.B., Wemmer, D.E., and James, T.L. (1995). Interproton distance bounds from 2D NOE intensities: effect of experimental noise and peak integration errors. J. Biomol. NMR *6,* 390-402.

Loewen, C.J., Gaspar, M.L., Jesch, S.A., Delon, C., Ktistakis, N.T., Henry, S.A., and Levine, T.P. (2004). Phospholipid metabolism regulated by a transcription factor sensing phosphatidic acid. Science *304,* 1644-1647.

Loewen, C.J., Roy, A., and Levine, T.P. (2003). A conserved ER targeting motif in three families of lipid binding proteins and in Opi1p binds VAP. EMBO J. *22,* 2025-2035.

Macura, S., Huang, Y., Suter, D., and Ernst, R.R. (1981). Two-dimensional chemical exchange and cross-relaxation spectroscopy of coupled nuclear spins. J. Magn. Reson. *43,* 259-281.

Murata, S., Mizumura, Y., Hino, K., Ueno, Y., Ichikawa, S., and Matsuda, A. (2007). Modular bent DNAs: a new class of artificial DNAs with a protein binding ability. J. Am. Chem. Soc. *129,* 10300-10301.

Nightingale, K., Dimitrov, S., Reeves, R., and Wolffe, A.P. (1996). Evidence for a shared structural role for HMG1 and linker histones B4 and H1 in organizing chromatin. EMBO J. *15,* 548-561.

Nishimura, A.L., Mitne-Neto, M., Silva, H.C., Richieri-Costa, A., Middleton, S., Cascio, D., Kok, F., Oliveira, J.R., Gillingwater, T., Webb, J., Skehel, P., and Zatz, M. (2004). A mutation in the vesicle-trafficking protein VAPB causes late-onset spinal muscular atrophy and amyotrophic lateral sclerosis. Am. J. Hum. Genet. *75,* 822-831.

Nishimura, Y., Hayashi, M., Inada, H., and Tanaka, T. (1999). Molecular cloning and characterization of mammalian homologues of vesicle-associated membrane protein-associated (VAMP-associated) proteins. Biochem. Biophys. Res. Commun. *254,* 21-26.

Ohndorf, U.M., Rould, M.A., He, Q., Pabo, C.O., and Lippard, S.J. (1999). Basis for recognition of cisplatin-modified DNA by high-mobility-group proteins. Nature *399,* 708-712.

Olkkonen, V.M., Johansson, M., Suchanek, M., Yan, D., Hynynen, R., Ehnholm, C., Jauhiainen, M., Thiele, C., and Lehto, M. (2006). The OSBP-related proteins (ORPs): global sterol sensors for co-ordination of cellular lipid metabolism, membrane trafficking and signalling processes? Biochem. Soc. Trans. *34,* 389-391.

Onufriev, A., Bashford, D., and Case, D.A. (2004). Exploring protein native states and large-scale conformational changes with a modified generalized born model. Proteins *55,* 383-394.

Palmer, A.G., Wright, P.E., and Rance, M. (1991). Measurement of relaxation time constants for methyl groups by proton-detected heteronuclear NMR spectroscopy. Chem. Phys. Lett. *185,* 41-46.

Pearlman, D.A., Case, D.A., Caldwell, J.W., Ross, W.S., Cheatham, T.E.I., DeBolt, S., Ferguson, D., Seibel, D., and Kollman, P. (1995). AMBER, a package of computer programs for applying molecular mechanics, normal mode analysis, molecular dynamics and free energy calculations to simulate the structural and energetic properties of molecules. Comp. Phys. Commun. *91,* 1-41.

Pennetta, G., Hiesinger, P.R., Fabian-Fine, R., Meinertzhagen, I.A., and Bellen, H.J. (2002). Drosophila VAP-33A directs bouton formation at neuromuscular junctions in a dosage-dependent manner. Neuron *35,* 291-306.

Perry, R.J., and Ridgway, N.D. (2006). Oxysterol-binding protein and vesicle-associated membrane protein-associated protein are required for sterol-dependent activation of the ceramide transport protein. Mol. Biol. Cell *17,* 2604-2616.

Piotto, M., Saudek, V., and Sklenar, V. (1992). Gradient-tailored excitation for single-quantum NMR spectroscopy of aqueous solutions. J. Biomol. NMR *2,* 661-665.

Pisetsky, D.S., Erlandsson-Harris, H., and Andersson, U. (2008). High-mobility group box protein 1 (HMGB1): an alarmin mediating the pathogenesis of rheumatic disease. Arthritis Res. Ther. *10,* 209.

P-ohler, J.R., Norman, D.G., Bramham, J., Bianchi, M.E., and Lilley, D.M. (1998). HMG box proteins bind to four-way DNA junctions in their open conformation. EMBO J. *17,* 817-826.

Rance, M., Sorensen, O.W., Bodenhausen, G., Wagner, G., Ernst, R.R., and Wuthrich, K. (1983). Improved spectral resolution in cosy ^{1}H NMR spectra of proteins via double quantum filtering. Biochem. Biophys. Res. Commun. *117,* 479-485.

Ridgway, N.D. (1995). 25-Hydroxycholesterol stimulates sphingomyelin synthesis in Chinese hamster ovary cells. J. Lipid Res. *36,* 1345-1358.

Ridgway, N.D., Dawson, P.A., Ho, Y.K., Brown, M.S., and Goldstein, J.L. (1992). Translocation of oxysterol binding protein to Golgi apparatus triggered by ligand binding. J. Cell Biol. *116,* 307-319.

Ryabov, Y.E., Geraghty, C., Varshney, A., and Fushman, D. (2006). An efficient computational method for predicting rotational diffusion tensors of globular proteins using an ellipsoid representation. J. Am. Chem. Soc. *128,* 15432-15444.

Salerno, W.J., Seaver, S.M., Armstrong, B.R., and Radhakrishnan, I. (2004). MONSTER: inferring non-covalent interactions in macromolecular structures from atomic coordinate data. Nucleic Acids Res. *32,* W566-8.

Sattler, M. S., Schleucher, J., and Griesinger, C. (1999). Heteronuclear multidimensional NMR experiments for the structure determination of proteins in solution employing pulsed field gradients. Prog. Nucl. Magn. Reson. Spectrosc. *34*, 93-158.

Schroter, H., and Bode, J. (1982). The binding sites for large and small high-mobility-group (HMG) proteins. Studies on HMG-nucleosome interactions in vitro. Eur. J. Biochem. *127,* 429-436.

Shoemaker, B.A., Portman, J.J., and Wolynes, P.G. (2000). Speeding molecular recognition by using the folding funnel: the fly-casting mechanism. Proc. Natl. Acad. Sci. U. S. A. *97,* 8868-8873.

Skehel, P.A., Fabian-Fine, R., and Kandel, E.R. (2000). Mouse VAP33 is associated with the endoplasmic reticulum and microtubules. Proc. Natl. Acad. Sci. U. S. A. *97,* 1101-1106.

Skehel, P.A., Martin, K.C., Kandel, E.R., and Bartsch, D. (1995). A VAMP-binding protein from Aplysia required for neurotransmitter release. Science *269,* 1580-1583.

Skelenar, V., and Bax, A. (1987). Spin-echo water suppression for the generation of pure-phase two-dimensional NMR spectra. J. Magn. Reson. *74,* 469-479.

Soussan, L., Burakov, D., Daniels, M.P., Toister-Achituv, M., Porat, A., Yarden, Y., and Elazar, Z. (1999). ERG30, a VAP-33-related protein, functions in protein transport mediated by COPI vesicles. J. Cell Biol. *146,* 301-311.

Stott, K., Tang, G.S., Lee, K.B., and Thomas, J.O. (2006). Structure of a complex of tandem HMG boxes and DNA. J. Mol. Biol. *360,* 90-104.

Su, X.C., Jergic, S., Ozawa, K., Burns, N.D., Dixon, N.E., and Otting, G. (2007). Measurement of dissociation constants of high-molecular weight protein-protein complexes by transferred 15N-relaxation. J. Biomol. NMR *38,* 65-72.

Tarr, D.E., and Scott, A.L. (2005). MSP domain proteins. Trends Parasitol. *21,* 224-231.

Thomas, J.O., and Travers, A.A. (2001). HMG1 and 2, and related 'architectural' DNA-binding proteins. Trends Biochem. Sci. *26,* 167-174.

Wang, C., JeBailey, L., and Ridgway, N.D. (2002). Oxysterol-binding-protein (OSBP)-related protein 4 binds 25-hydroxycholesterol and interacts with vimentin intermediate filaments. Biochem. J. *361,* 461-472.

Wang, P.Y., Weng, J., and Anderson, R.G. (2005). OSBP is a cholesterol-regulated scaffolding protein in control of ERK 1/2 activation. Science *307,* 1472-1476.

Webb, M., Payet, D., Lee, K.B., Travers, A.A., and Thomas, J.O. (2001). Structural requirements for cooperative binding of HMG1 to DNA minicircles. J. Mol. Biol. *309,* 79-88.

Weir, M.L., Klip, A., and Trimble, W.S. (1998). Identification of a human homologue of the vesicle-associated membrane protein (VAMP)-associated protein of 33 kDa (VAP-33): a broadly expressed protein that binds to VAMP. Biochem. J. *333 (Pt 2),* 247-251.

Weir, M.L., Xie, H., Klip, A., and Trimble, W.S. (2001). VAP-A binds promiscuously to both v- and tSNAREs. Biochem. Biophys. Res. Commun. *286,* 616-621.

Werner, M.H., Huth, J.R., Gronenborn, A.M., and Clore, G.M. (1995). Molecular basis of human 46X,Y sex reversal revealed from the three-dimensional solution structure of the human SRY-DNA complex. Cell *81,* 705-714.

Wolfe, S.A., Ferentz, A.E., Grantcharova, V., Churchill, M.E., and Verdine, G.L. (1995). Modifying the helical structure of DNA by design: recruitment of an architecture-specific protein to an enforced DNA bend. Chem. Biol. *2,* 213-221.

Wright P. E. and Dyson HJ (1999). Intrinsically unstructured proteins: re-assessing the protein structure–function paradigm**.** J. Mol. Biol. *293*, 321-331.

Wyles, J.P., McMaster, C.R., and Ridgway, N.D. (2002). Vesicle-associated membrane protein-associated protein-A (VAP-A) interacts with the oxysterol-binding protein to modify export from the endoplasmic reticulum. J. Biol. Chem. *277,* 29908-29918.

Wyles, J.P., and Ridgway, N.D. (2004). VAMP-associated protein-A regulates partitioning of oxysterol-binding protein-related protein-9 between the endoplasmic reticulum and Golgi apparatus. Exp. Cell Res. *297,* 533-547.

Xu, Y., Liu, Y., Ridgway, N.D., and McMaster, C.R. (2001). Novel members of the human oxysterol-binding protein family bind phospholipids and regulate vesicle transport. J. Biol. Chem. *276,* 18407-18414.

Yang, H. (2006). Nonvesicular sterol transport: two protein families and a sterol sensor? Trends Cell Biol. *16,* 427-432.

6. Appendix

DNA recognition mechanism by High mobility group box 1

6.1 Introduction

DNA binding proteins recognize DNA sequences or higher-order structures of DNAs. Structure specific protein-DNA interactions are involved in many important events, such as transcription, DNA replication, and DNA repair. However, structure-specific DNA recognition mechanism is less understood than sequence-specific DNA recognition (Garvie, C.W. and Wolberger, C., 2001) because of difficulty due to instabilities of higher-order DNA structures (P-ohler, J.R. *et. al.*, 1998; Wolfe, S.A. *et. al.*, 1995).

High mobility group box 1 (HMGB1) is a well-known structure specific DNA binding protein. HMGB1 consists of 2 DNA binding HMG domains, called A-box and B-box, and the C-terminal acidic region (Appendix Figure 1) (Thomas, J.O. and Travers, A.A., 2001). Many studies have been conducted about the interaction of HMGB1 with DNA. HMGB1 is known to bind preferentially to distorted DNA structures. For example, it binds bent DNA such as cisplatin (CP) linked DNA (Hughes, E.N. *et. al.*, 1992), four-way junction (Bianchi, M.E., 1988; Bianchi, M.E., 1989), and DNA mini-circles (Webb, M. *et. al.*, 2001).

HMGB1 has a dual function. First, inside the cell, HMGB1 regulates transcription. HMGB1 binds nucleosome and enhances nucleosome sliding (Schroter, H. and Bode, J., 1982; Nightingale, K. *et. al.*, 1996; Catez, F. *et. al.*, 2004). HMGB1 also binds promoter regions of DNA and facilitates association of transcription factors (Das, D. and Scovell, W. M., 2001). Second, outside the cell, HMGB1 acts as an inflammatory mediator. HMGB1 is released from activated immune cells and necrotic cells. Extra cellular HMGB1 interacts with cell surface receptors of target cells, enhances inflammatory responses such as inflammatory

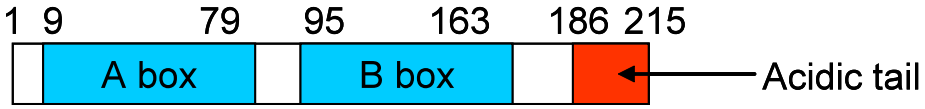

Appendix Figure 1. Domain structure of human HMGB1.

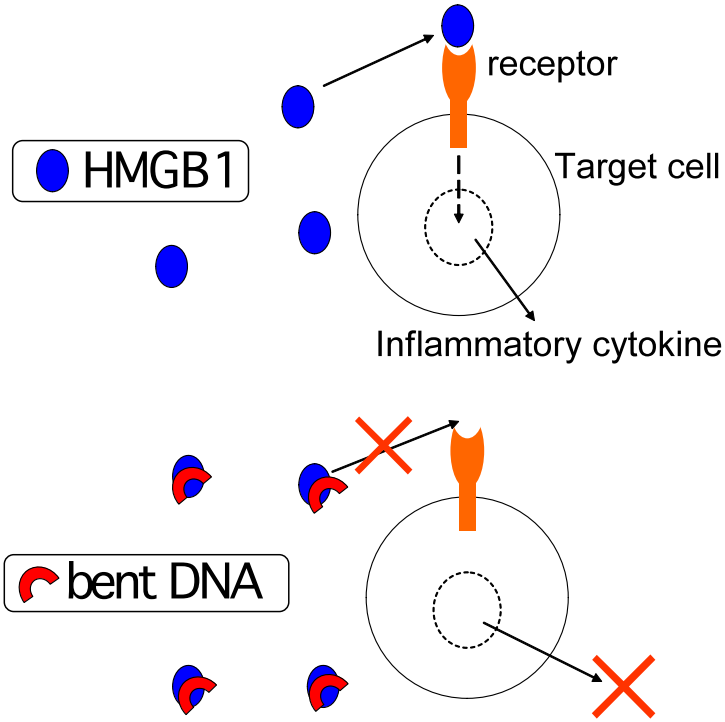

Appendix Figure 2. Function of extra cellular HMGB1 (upper figure), and expected effect of bent DNA on inhibition of interactions between HMGB1 and the receptors (lower figure).

cytokine production (Appendix Figure 2, upper figure), and is involved in onsets of inflammatory diseases (Klune, J.R. et. al., 2008; Pisetsky, D.S. *et. al.*, 2008). Bent DNA is known to strongly bind to HMGB1. Therefore, administration of bent DNA is expected to inhibit the interaction of HMGB1 with the receptor, and improve inflammatory diseases (Appendix Figure 2, lower figure).

Recently, novel DNA oligomers were synthesized for a study of structure specific DNA recognition and anti-inflammatory medication targeting HMGB1 (Murata, S. *et. al.*, 2007). They contain cyclic 2'-deoxyuridylate dimmers, which possess ethylene ($U^{et}_{p}U$) or propylene linkages ($U^{pr}_{p}U$) (Appendix Figure 3). For these DNA oligomers, bending angles were estimated by FRET experiments and both were considered to have large bending angles of about 90 degree. However, their binding affinities for HMGB1 A-box were quite different. Gel shift assays showed that the $U^{et}_{p}U$ DNA oligomer strongly binds to HMGB1 with a dissociation constant of about 2 nM, whereas binding between the $U^{pr}_{p}U$ DNA oligomer and HMGB1 was not detected (Murata, S. *et. al.*, 2007). I have analyzed NMR structures of the $U^{et}_{p}U$ and $U^{pr}_{p}U$ DNA oligomers in order to clarify the difference in affinity for HMGB1 A-box (Appendix Figure 4).

6.2 Materials and Methods

6.2.1 Sample preparations

DNA oligomers containing $U^{et}_{p}U$ and $U^{pr}_{p}U$ were gifted from Drs. Shunpei Murata, Satoshi Ichikawa and Akira Matsuda (Faculty of Pharmaceutical Sciences, Hokkaido University). Recombinant HMGB1 A-box protein (WT and F38A) for titration experiments were prepared as follows. DNA fragments encoding human HMGB1 (residues M1-F89) were amplified from QUICK-Clone™ cDNAs (CloneTech), and subsequently cloned into the

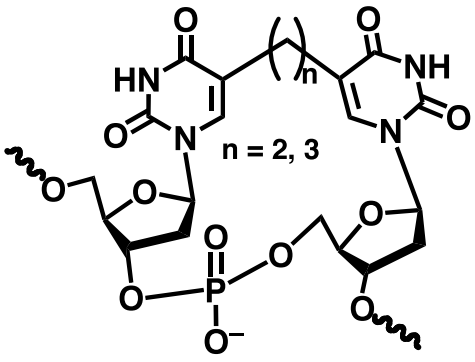

Appendix Figure 3. Structure of alkylene cross-linked cyclic 2'-deoxyuridylate. n=2, $U^{et}_{p}U$; n=3, $U^{pr}_{p}U$.

5 ' - C C T T C A U U A C A T C C - 3 '
3 ' - G G A A G T A A T G T A G G - 5 '

Appendix Figure 4. Sequence of DNA oligomers used in this study. Alkylene cross-linked cyclic 2'-deoxyuridylate is shown in red.

pGEX-6P-3 expression vector. The expression vector for F38A mutant of HMGB1 was prepared using QuikChange (Stratagene). ^{15}N-labeled HMGB1 (WT and F38A) were over-expressed in E. coli Rosetta (DE3) in M9 medium containing $^{15}NH_4Cl$ and unlabeled glucose. Cells expressing HMGB1 (WT and F38A) were lysed by sonication in a buffer containing 50 mM Tris-HCl (pH 8.0), 300 mM NaCl, 5 mM DTT and 0.1 mM EDTA. The lysate was centrifuged at 35,000 rpm for 30 min at 4°C. The supernatant was mixed with polyethyleneimine to the final concentration of 0.5% and put on ice for 15 minutes, then it was centrifuged again and the supernatant was loaded onto a glutathione Sepharose 4B resin (GE Healthcare). The resin was washed with a buffer solution containing 1M NaCl, and subsequently protein was eluted with buffer containing 10 mM glutathione. The eluate was concentrated and the GST tag was removed using HRV3C Protease. Finally, protein was purified on a Superdex 75 (26/ 60) gel filtration column (GE Healthcare) equilibrated with buffer containing 20 mM sodium phosphate (pH 6.8), 100 mM NaCl, 0.1 mM EDTA and 1 mM DTT.

6.2.2 NMR experiments

All NMR spectra were measured by AV500 or DRX800 spectrometers (Bruker), processed using NMRpipe (Delaglio, F. *et. al.*, 1995) and analyzed using SPARKY (Goddard and Kneller, UCSF). NMR samples of the $U^{pr}_{p}U$ and $U^{et}_{p}U$ DNA oligomers for structural analyses were prepared at the concentrations of about 0.7 mM $U^{et}_{p}U$ or 0.5 mM $U^{pr}_{p}U$ DNA oligomers in 90%/10% H_2O/D_2O or 100% D_2O containing 20 mM sodium phosphate (pH 6.8), 100 mM sodium chloride and 0.1 mM EDTA. For the samples of DNA oligomers in 90%/10% H_2O/D_2O, the following spectra were recorded: 1-1 echo 1D spectra (Sklenar, V. and Bax, A., 1987) at various temperatures (278, 283, 288, 293, 298, 303, 308, 313, 318, 323 K), ^{1}H-^{1}H NOESY spectra with a WATERGATE sequence (Macura, S. *et. al.*, 1981; Piotto,

M. *et. al*., 1992) at 275K with mixing time 100 msec, at 283K with mixing time 120 msec, and at 303K with mixing times 30 and 200 msec, TOCSY spectra (Braunschweiler, L. and Ernst, R.R., 1983) at 303K with mixing time 33 msec and DQF-COSY spectra (Rance, M. *et. al.*, 1983) at 303K. For the samples in 100% D_2O, the following spectra were recorded: ^1H-^1H NOESY spectra at 283K with mixing time 120 msec and natural abundance ^1H-^{13}C HSQC spectra (Bodenhausen, G. and Ruben, D. J., 1980) at 303K.

NMR titration experiments of the U^{et}_pU and U^{pr}_pU DNA oligomers with HMGB1 A-box (WT and F38A) were performed in 90% H_2O / 10% D_2O (v/v) containing 20 mM sodium phosphate (pH 6.8), 100 mM sodium chloride, 1 mM DTT and 0.1 mM EDTA. Initial concentrations of the DNA oligomers were set to about 75 μM and 50 μM for titration experiments with WT and F38A, respectively. The experiments were carried out at 283 K using 1D 1-1 echo pulse sequence. The proteins were added until the molar ratio of DNA oligomers to proteins reaches 1:2.

6.2.3 Chemical shift assignments

Chemical shift assignments of the U^{et}_pU and U^{pr}_pU DNA oligomers were initially made using spectra measured at 303 K; ^1H-^1H NOESY, 2D TOCSY, and natural abundance ^1H-^{13}C HSQC spectra. Stereospecific assignments of H2' and H2" were obtained on the basis of the intensity of their NOEs to H1' in the ^1H-^1H NOESY spectra with mixing time of 30 msec. ^1H-^{13}C HSQC spectra were used to confirm assignments of protons in alkylene linkages. Then, chemical shift assignments at 283 K were made using ^1H-^1H NOESY spectra measured in 90/10% H_2O/D_2O and 100% D_2O at 283 K, referring the assignments at 303 K.

6.2.4 Structure determinations

Distance restraints of the U^{et}_pU and U^{pr}_pU DNA oligomers were obtained from ^1H-^1H

NOESY spectra with mixing time 120 msec measured at 283K in 90/10% H_2O/D_2O and 100% D_2O. Cross-peaks in each spectrum was integrated using SPARKY (Goddard and Kneller, UCSF), then distance restraints were obtained from the integration values using the complete relaxation matrix analysis program MARDIGRAS (Borgias, B.A. and James, T.L., 1989). Calculations were run with 4 ns correlation time, assuming isotropic tumbling. The errors were generated by RANDMARDI mode with 50 iterations (Liu, H. *et. al*., 1995). For the cross-peaks in ^1H-^1H NOESY spectra measured in 100% D_2O, the values of 'low1' and 'up2' given by MARDIGRAS calculations were used as upper and lower bounds of the constraint. For the ^1H-^1H NOESY spectra in 90/10% H_2O/D_2O, only restraints containing imino-proton which 'up2' values were less than 5.0 were used, and upper and lower limits were set to 5.0 and 1.8 Å, respectively. Sugar conformations were estimated from H1-H2' and H1-H2" cross-peak patterns in DQF-COSY spectra, and U7 was considered to have the N-type conformer, and the others were considered to have S-type conformers.

In order to obtain force fields for the U^{et}_pU and U^{pr}_pU DNA oligomers, first, we created the coordinates of the U^{et}_pU and U^{pr}_pU DNA oligomers by using xLEaP of AMBER package (Pearlman, D.A. *et. al.*, 1995). Second, new parameters for the bonds and angles in the DNA were generated by PRODRG2 server (http://davapc1.bioch.dundee.ac.uk/prodrg/). Then, the parameters were modified to be compatible with CNS commands. The initial structures of the U^{et}_pU and U^{pr}_pU were generated by CNS 1.2 (Brunger, A.T., *et. al.*, 1998; Brunger, A.T., 2007) as extended models. Structure calculations were performed by CNS 1.2. Since structural parameters for deoxyribose supplied with CNS restricts sugar conformer to S-type, modified parameter, where sugar conformation of U7 was restricted to N-type, was used for the structure determinations. Other than experimental distance restraints, B-type dihedral angle constraints for backbone angles (α=-60°, β=180°, γ=60°, δ=145°, ε=-180°, ζ=-85°) were entered with boundaries of ±15°, except for U7. Six distance restraints per base

pair were employed to describe the Watson-Crick base pairing; for G·C base-pairs, $r_{N1\text{-}N3}$=2.87 Å, $r_{H1\text{-}N3}$=1.86 Å, $r_{O6\text{-}N4}$=2.81 Å, $r_{N2\text{-}O2}$=2.81 Å, $r_{O6\text{-}N3}$=3.58 Å, and $r_{N2\text{-}N3}$=3.63 Å; for A·T base-pairs, $r_{N1\text{-}N3}$=2.92 Å, $r_{N1\text{-}H3}$=1.87 Å, $r_{N6\text{-}O4}$=2.89 Å, $r_{H2\text{-}O2}$=2.94 Å, $r_{N6\text{-}O4}$=3.69 Å, and $r_{N1\text{-}O2}$=3.67 Å, with errors of +0.5 and –0.2 Å for U7-A22 and U8-A21 base pairs, and ±0.2 Å for the others. Base planarity restraints were entered with the force constant of 2 kcal mol^{-1} $Å^{-2}$ for U7-A21 and U8-A22 base-pairs, and 5 kcal mol^{-1} $Å^{-2}$ for the others. In the high temperature stage, the structures were heated to 20,000 K in torsion angle space for 240 ps with 16,000 steps, 0.1 kcal mol^{-1} $Å^{-4}$ for the van der Waals repulsion term, 60 kcal mol^{-1} $Å^{-2}$ for experimental distance restraints, and 5 kcal mol^{-1} rad^{-2} for dihedral restraints. In the first slow-cooling stage, the structures heated to 20,000 K and then cooled for 80 ps with 8,000 steps, 150 K drops for each cycle of dynamics, 1.0 kcal mol^{-1} $Å^{-4}$ for the van der Waals repulsion term, 60 kcal mol^{-1} $Å^{-2}$ for experimental distance restraints, and 100 kcal mol^{-1} rad^{-2} for dihedral restraints. In the second slow-cooling stage, the structures heated to 2,000 K for 36 ps with 12,000 steps, 15 K drops for each cycle of dynamics, 1.0 to 4.0 kcal mol^{-1} $Å^{-4}$ for the van der Waals repulsion term, 60 kcal mol^{-1} $Å^{-2}$ for experimental distance restraints, and 100 kcal mol^{-1} rad^{-2} for dihedral restraints. Finally, structures were minimized during 10 cycles of 200 steps with experimental distance restraints and dihedral force constants of 30 kcal mol^{-1} $Å^{-2}$ and 200 kcal mol^{-1} rad^{-2}, respectively. For the $U^{et}{}_pU$ and $U^{pr}{}_pU$ DNA oligomers, 300 structures were calculated and 20 structures with the lowest energy were selected. Analysis of the final 20 structures was carried out by the programs Curves V5.1 (Lavery, R. and Sklenar, H., 1989).

6.3 Results

6.3.1 Chemical shift assignments

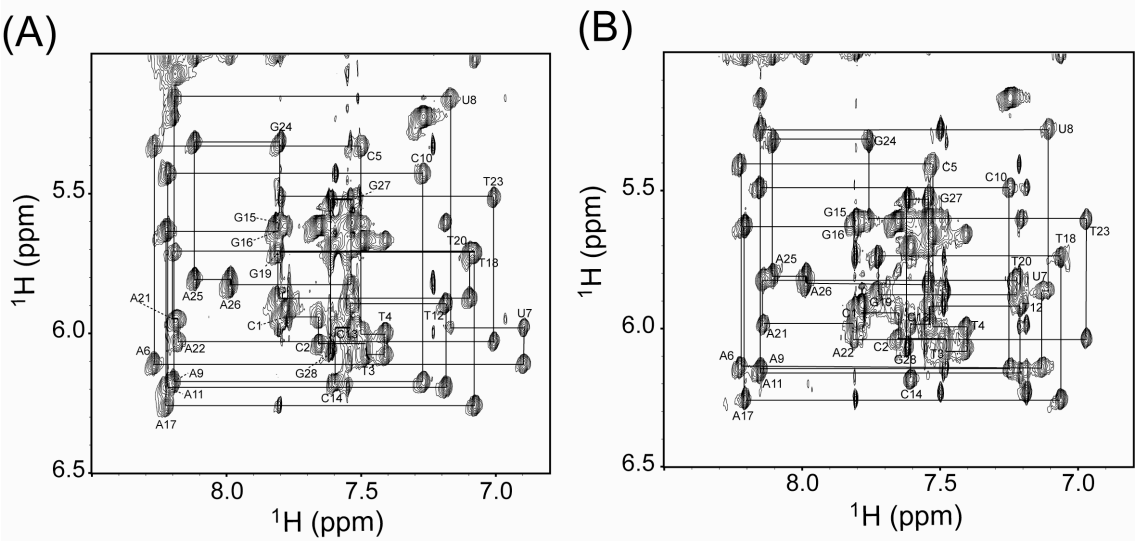

Appendix Figure 5. Base H6/H8 and suger H1' region of ^{1}H-^{1}H NOESY spectra of the U^{et}_pU (A) and U^{pr}_pU (B) oligomers recorded at 283 K in 100% D_2O. Intraresidue NOE cross peaks between H6/H8 and H1' are labelled with their residue numbers.

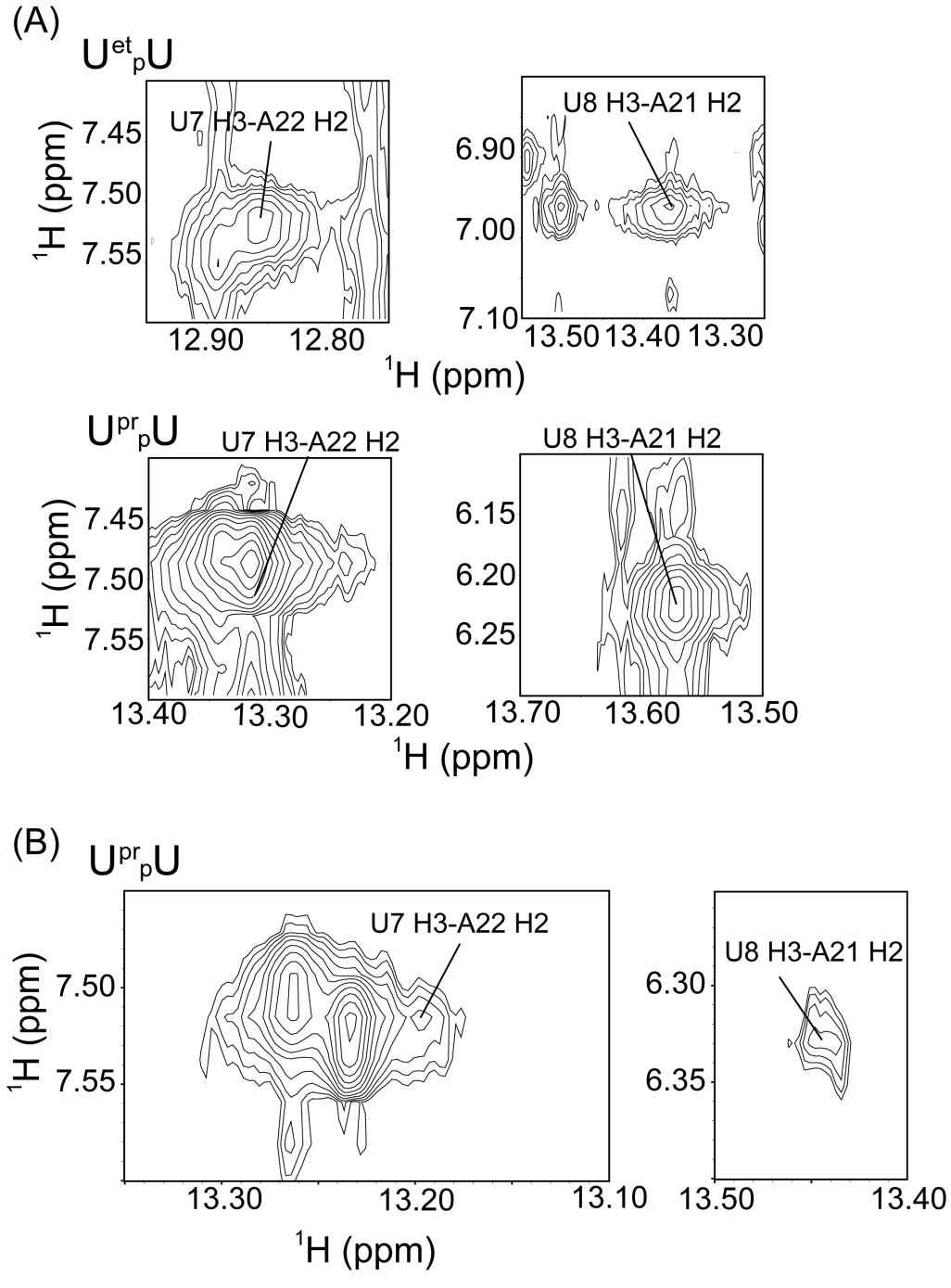

Appendix Figure 6. (A) NOE peaks between U7 H3-A22 H2 and U8 H3-A21 H2 in the ^{1}H-^{1}H NOESY spectra of the U$^{et}_{p}$U (upper) and U$^{pr}_{p}$U (lower) DNA oligomers recorded at 283 K. (B) NOE peaks between U7 H3-A22 H2 and U8 H3-A21 H2 in the ^{1}H-^{1}H NOESY spectrum of the U$^{pr}_{p}$U DNA oligomer recorded at 303 K.

For the U^{et}_pU and U^{pr}_pU DNA oligomers, we assigned most of proton resonances at 283 K, with the exception of H4', H5'/H5", and NH_2 of guanine. Appendix Figures 5A and 5B show sequential connectivities between base H6/H8 and suger H1' protons for ^1H-^1H NOESY spectra of the U^{et}_pU and U^{pr}_pU DNA oligomers, respectively. Both DNA oligomers showed NOE peaks between U7 H3-A22 H2, and U8 H3-A21 H2 in the ^1H-^1H NOESY spectra recorded at 283K in 90/10% H_2O/D_2O, indicating that alkylene linkages do not disrupt U7-A22 and U8-A21 base pairs at 283K (Appendix Figure 6A). In ^1H-^1H NOESY spectra recorded at 303 K, these NOE peaks were observed for the U^{pr}_pU DNA oligomer, but not for the U^{et}_pU DNA oligomer (Appendix Figure 6B). This indicates that U7-A22 and U8-A21 base pairs in the U^{pr}_pU DNA oligomer are stabler than those in the U^{et}_pU DNA oligomer.

6.3.2 Structure determinations and global structures

Structure calculations of the U^{et}_pU and U^{pr}_pU were performed using CNS 1.2 with 309 and 307 experimental distance restraints, respectively. Except for the experimental distance restraints, the same restrains and annealing protocol were used for calculations of these DNA oligomers. Because both DNA oligomers were assumed to have right-handed B-form like structures judged from cross-peak patterns in NOESY and DQF-COSY spectra, B-form like constraints for backbone angles were entered with boundaries of ±15°, except for U7, which has a S-type sugar conformation. Restraints used for the calculations were summarized in Appendix Table 1. Appendix Figures 7A and 7B show superimposed pictures of final 20 structures of the U^{et}_pU and U^{pr}_pU DNA oligomers, respectively. Structural statistics for the final structures are shown in Appendix Table 1. A21 H2 of the U^{pr}_pU DNA oligomer showed up-field shift (6.231 ppm at 283 K). In the determined structure, this proton was located immediately above the aromatic ring of A9 (Appendix Figure 7C). The up-field shift of this proton is considered to be caused by the ring current effect. As shown in Appendix Figures

Appendix Table 1. Structural statistics for the $U^{et}_{p}U$ and $U^{pr}_{p}U$ DNA oligomers.

	$U^{et}_{p}U$	$U^{pr}_{p}U$
NOE distance restraitnt		
intraresidue	125	122
sequential	141	142
cross-strand	43	43
total	309	307
Empirical constraints		
hydrogen bonds	84	84
backbone dihedral angles	152	152
Structural statistics		
distance violation (> 0.5 Å)	0	0
dihedral angle violations (> 5°)	0	0
Structure quantity		
RSMD (all atom) (Å)	0.813	0.950

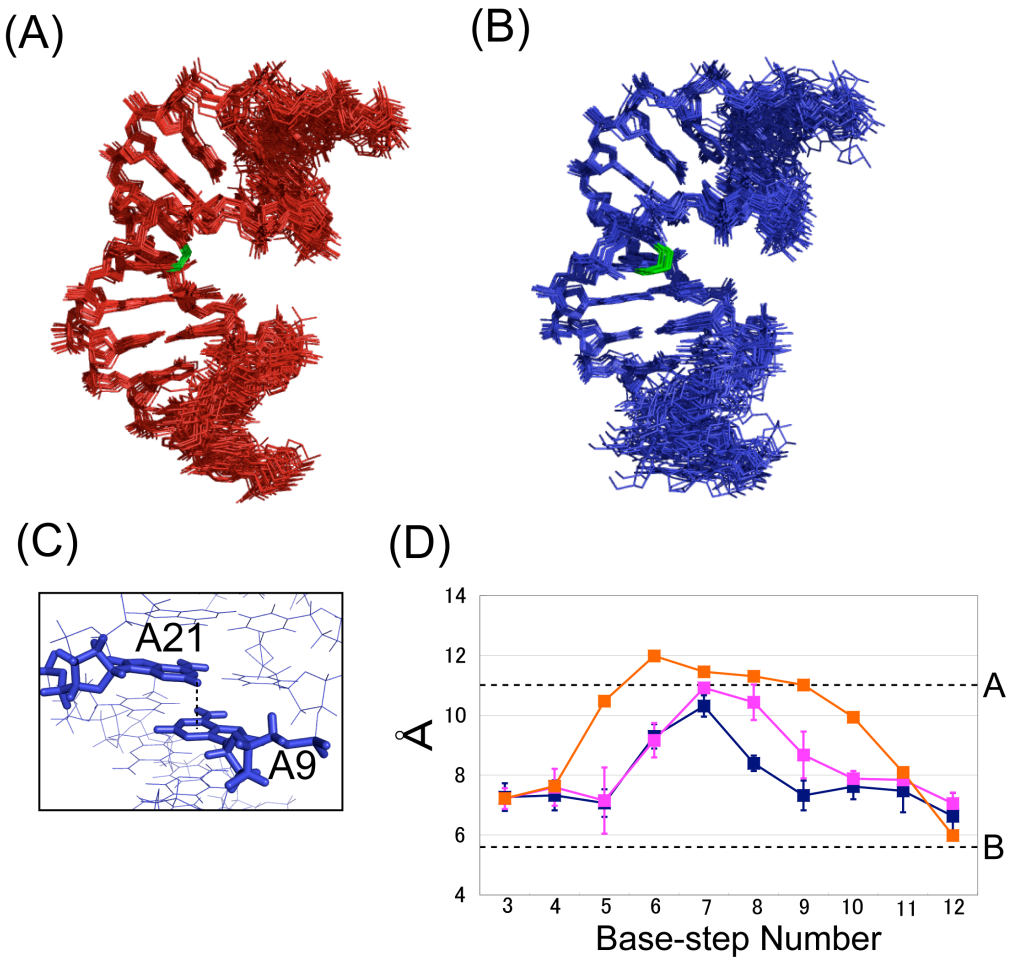

Appendix Figure 7. Superimposed representation of 20 lowest energy structures of the $U^{et}_{p}U$ (A) and $U^{pr}_{p}U$ (B) DNA oligomers. (C) A blow-up view of the lowest energy structure of the $U^{pr}_{p}U$ DNA oligomer around cross-linked site. A21 and A9 are shown by stick model. (D) Minor groove width of the $U^{et}_{p}U$ (pink) and $U^{pr}_{p}U$ (blue) oligomers, and cisplatin cross-linked DNA oligomer complexed with HMGB1 A-box (ogange) (PDB ID, 1CKT; Ohndorf, U.M. *et. al.*, 1999). Typical values of A- and B- form DNA are shown by dotted lines.

Appendix Table 2. Comparison of selected helical parameters around cross-linked site and overall bending angle for the $U^{et}_{p}U$ and $U^{pr}_{p}U$ DNA oligomers and CP linked DNA oligomer complexed with HMGB1 A-box (PDB ID, 1CKT; Ohndorf, U.M. *et. al.*, 1999) obtained using the programs Curves V5.1 (Lavery, R. and Sklenar, H., 1989). Base name of CP linked DNA oligomer is given in parentheses.

	$U^{et}_{p}U$	$U^{pr}_{p}U$	CP
A6-U7 (T6-G7)			
shift (Å)	0.23 ± 0.20	-0.32 ± 0.28	0.89
roll (deg)	-7.245 ± 4.27	-1.58 ± 2.79	-17.31
twist (deg)	37.77 ± 2.72	25.30 ± 5.97	37.52
U7-U8 (G7-G8)			
shift (Å)	-0.13 ± 0.24	0.877 ± 0.24	-0.55
roll (deg)	37.41 ± 1.66	19.61 ± 1.97	67.45
twist (deg)	13.94 ± 3.21	33.96 ± 4.16	11.48
U8-A9 (G8-A9)			
shift (Å)	0.44 ± 0.16	-0.07 ± 0.13	-0.28
roll (deg)	-2.30 ± 4.4	0.48 ± 3.31	-6.42
twist (deg)	40.21 ± 2.82	35.8 ± 2.08	36.79
bending angle (deg)	46.7 ± 6.1	39.1 ± 8.7	61.1

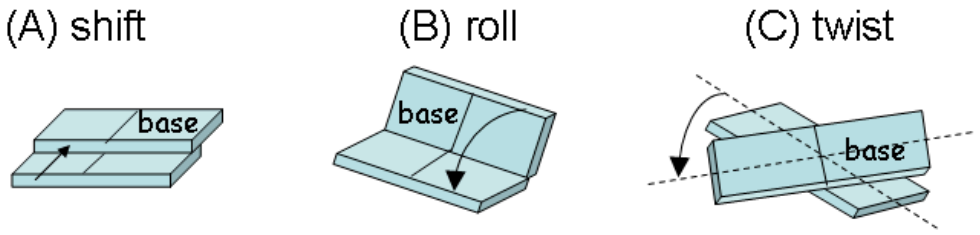

Appendix Figure 8. Definitions of the helical parameters in the Appendix table 2. (A) shift, (B) roll, (C) twist.

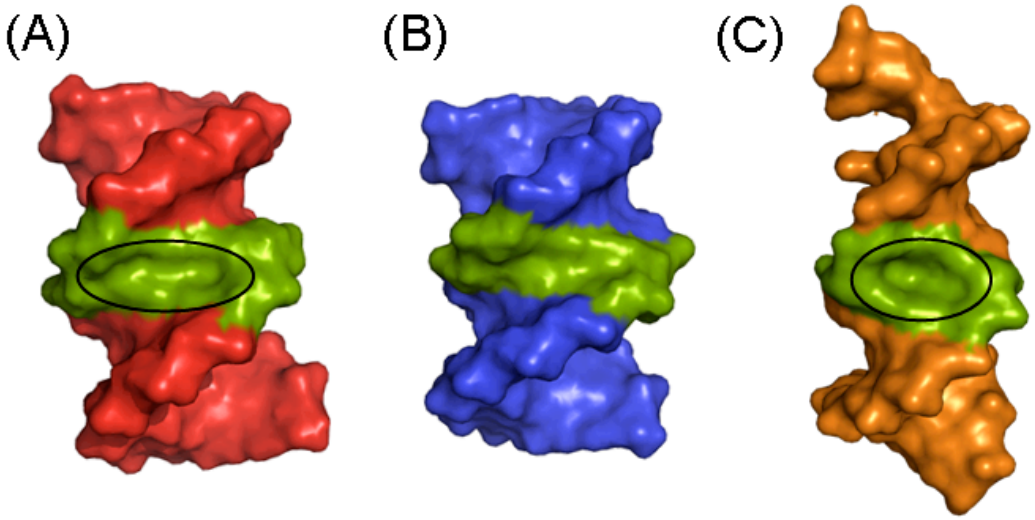

Appendix Figure 9. Surface representations of the lowest energy structures of the $U^{et}_{p}U$ (A) and $U^{pr}_{p}U$ (B) DNA oligomers, and CP linked DNA oligomer complexed with HMGB1 A-box (PDB ID, 1CKT; Ohndorf, U.M. *et. al.*, 1999) (C). Cross-linked residues and the complementary residues shown in green. Pockets observed in the cross-linked sites are indicated by circles.

7A and 7B, both DNA oligomers have right-handed B-form like structures bended around cross-linked site, and their bending angles were 47 ±6 and 39 ±9 °, respectively. Appendix Figure 7D shows minor groove width of these DNA oligomers. Both DNA oligomers have wider minor grooves than regular B-form DNA.

6.3.3 Comparison of local structures around cross-linked site

Selected helical parameters around cross-linked site are shown in Appendix Table 2. Helical parameters are used to describe structure of nucleic acid double helices (Appendix Figure 8). The $U^{et}_{p}U$ DNA oligomer has small twist angles at cross-linked site, whereas the $U^{pr}_{p}U$ DNA oligomer does not. The $U^{et}_{p}U$ DNA oligomer has the larger roll angle at the cross-linked site than the $U^{pr}_{p}U$ DNA oligomer. The $U^{pr}_{p}U$ DNA oligomer shows a large positive shift value at cross-linked site, whereas the $U^{et}_{p}U$ DNA oligomer does not. These parameters suggest that the $U^{et}_{p}U$ DNA oligomer bends by large roll combined with unwinding at the cross-linked site, whereas the $U^{pr}_{p}U$ DNA oligomer bends by large shift with roll. The structural differences can be shown graphically as surface representations (Appendix Figures 9A and 9B). The $U^{et}_{p}U$ DNA oligomer has a pocket at the cross-linked site, whereas the $U^{pr}_{p}U$ DNA oligomer does not. The structure of the $U^{et}_{p}U$ DNA oligomer seemed to be destabilized by the pocket. Therefore, we examined thermal stabilities of these DNA oligomers by measuring 1D 1-1 echo NMR spectra at various temperatures. Appendix Figure 10 shows imino-proton regions of the $U^{et}_{p}U$ and $U^{pr}_{p}U$ DNA oligomers at various temperatures. At 323 K, some imino-proton peaks were observed for the $U^{pr}_{p}U$ DNA oligomer, but not for the $U^{et}_{p}U$ DNA oligomer. This indicates that the $U^{et}_{p}U$ DNA oligomer is less thermally stable than the $U^{pr}_{p}U$ DNA oligomer, consistent with the previous report (Murata, S. *et. al.*, 2007).

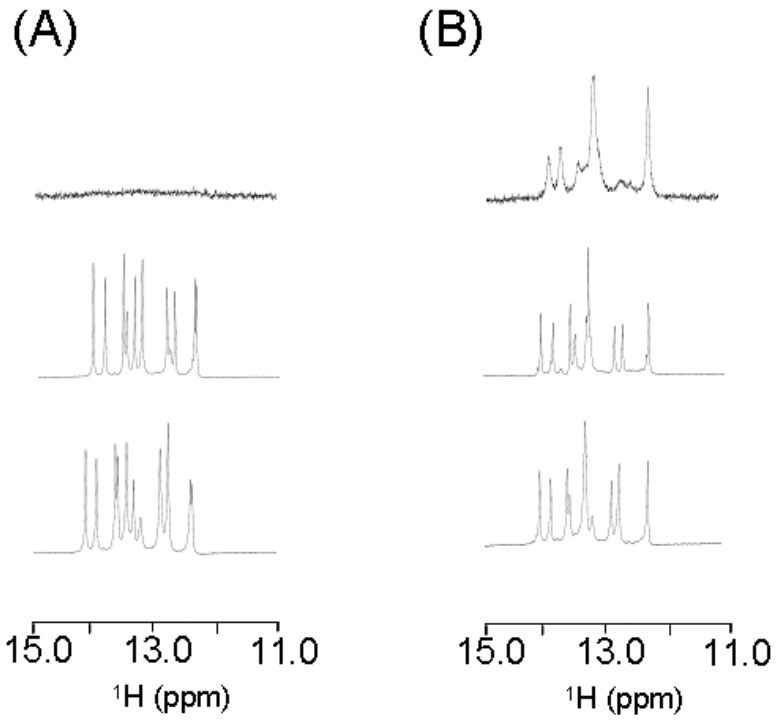

Appendix Figure 10. 1D 1-1 echo NMR spectra of the $U^{et}{}_pU$ and $U^{pr}{}_pU$ DNA oligomers at various temperatures. (bottom) 283 K, (middle) 303 K, (top) 323 K.

6.4 Discussion

6.4.1 Reason of the affinity difference; structure around cross-linked site

HMG domains consist of three α-helices arranged in an L-shape, and bind to the minor groove of DNA, where one or two hydrophobic residues intercalate between base-pairs (Thomas, J.O. and Travers, A.A., 2001). Upon binding, HMG domains expand the minor groove of DNA and introduce a large bent into DNA (Werner, M.H. *et. al.*, 1995; Ohndorf, U.M. *et. al.*, 1999; Stott, K. *et. al.*, 2006). Both $U^{et}_{p}U$ and $U^{pr}_{p}U$ DNA oligomers have wide minor grooves, and bend in their free states. However, the minor groove widths and the overall bending angles were not so different between these oligomers (Figure 7D, Table 2), Therefore these values will not explain the affinity difference for HMGB1 A-box protein.

When HMGB1 A-box binds DNA, the aromatic ring of the Phe residue located at the N-terminal end of the second helix intercalates between base-pairs (Ohndorf, U.M. *et. al.*, 1999). In a crystal structure of rat HMGB1 A-box complexed with CP linked DNA oligomer, this Phe residue intercalates within the G_pG CP cross-linked site, and the complex was stabilized by the stacking interactions between the Phe residue and cross-linked guanene bases (Appendix Figure 11) (Ohndorf, U.M. *et. al.*, 1999). Selected helical parameters around the cross-linked site of CP linked DNA oligomer complexed with HMGB1 A-box were shown in Appendix Table 2. The helical parameters are closer to the $U^{et}_{p}U$ DNA oligomer than the $U^{pr}_{p}U$ DNA oligomer. Figure 9C shows surface representation of the CP linked DNA oligomer complexed with HMGB1 A-box. Similar to the $U^{et}_{p}U$ DNA oligomer, the CP linked DNA oligomer has a pocket at the cross-linked site, into which the aromatic ring of the Phe residue of the HMGB1 A-box intercalates.

Comparison of structures around the cross-linked site between the $U^{et}_{p}U$ and $U^{pr}_{p}U$ DNA oligomers, together with CP linked DNA oligomer complexed with HMGB1 A-box

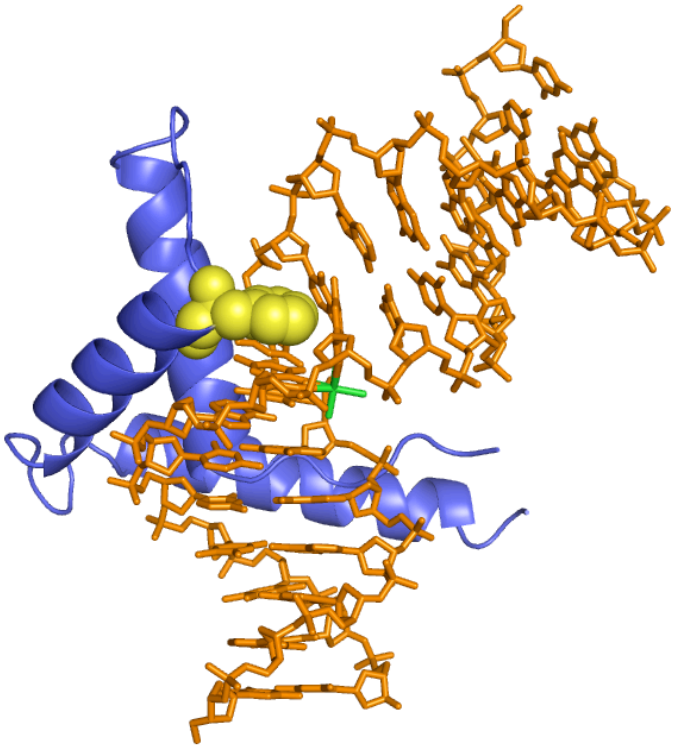

Appendix Figure 11. Crystal structure of the complex between HMGB1 A-box and CP linked DNA oligomer (PDB ID, 1CKT; Ohndorf, U.M. *et. al.*, 1999). HMGB1 A-box is shown in ribbon model. Phe residue which intercalates between base-pairs is shown by spheres. CP linkage is shown in green.

suggests that the interaction between the Phe residue in HMGB1 A-box and alkylene cross-linked DNA oligomer is important for their binding, and a pocket in DNA is important for the interaction. To confirm this, we compared binding affinities between the $U^{et}_{p}U$ and $U^{pr}_{p}U$ DNA oligomers and human HMGB1 A-box (WT) and the Ala mutant of Phe-38, which located at N-terminal end of the second helix. NMR titration experiments were performed in a buffer solution containing 20 mM sodium phosphate (pH 6.8), 100 mM sodium chloride and 0.1 mM EDTA and 1 mM DTT, using a 1D 1-1 echo pulse sequence at 283 K. Because most of the signals from DNA and proteins are highly overlapped in 1D ^{1}H NMR spectra of the complexes, we compared the imino-proton regions of these spectra. On addition of HMGB1 A-box (WT), some signals of the $U^{et}_{p}U$ DNA oligomer diminish, and new resonances appear and grow in intensity (Appendix Figure 12A). Some signals of the $U^{pr}_{p}U$ DNA oligomer are shifted (Appendix Figure 12B). These results indicate that HMGB1 A-box interacts with both DNA oligomers, but affinity for the $U^{et}_{p}U$ DNA oligomer is higher than the $U^{pr}_{p}U$ DNA oligomer. Because of resonance overlaps, it was not clear which imino-proton peaks underwent larger changes upon addition of HMGB1 A-box. In the case of titration experiments using the HMGB1 A-box F38A mutant, imino-proton peaks in both DNA oligomers became broader, and some peaks shifted (Appendix Figure 13A and 13B). These results indicate that the HMGB1 A-box F38A mutant can bind both DNA oligomers, but their affinities are much lower. After titration experiments, in order to eliminate effects of non-specific charge interactions, solvents of 1:2 mixture of DNA oligomer with protein were exchanged to a buffer containing high concentrations of salts (50 mM sodium phosphate (pH 6.8), 300 mM sodium chloride and 0.1 mM EDTA and 1 mM DTT). In this case, imino-proton peaks of the $U^{pr}_{p}U$ DNA oligomer with an excess amount of HMGB1 A-box WT, and the $U^{et}_{p}U$ and $U^{pr}_{p}U$ DNA oligomers with an excess amount of the HMGB1 A-box F38A mutant became sharp, and the positions were essentially same as in the free states,

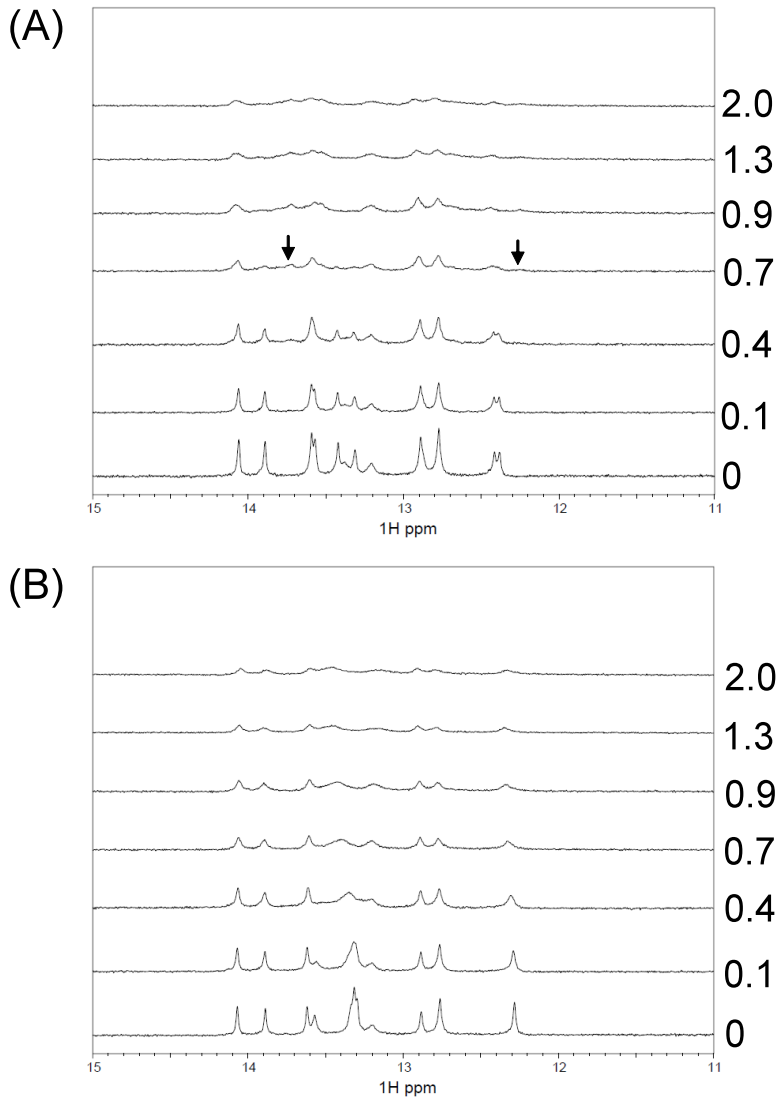

Appendix Figure 12. Titration experiments of the $U^{et}_{p}U$ (A) and $U^{pr}_{p}U$ (B) DNA oligomers with HMGB1 A-box (WT). Molar ratios of HMGB1 A-box to DNA oligomers are indicated on the right of spectra. Newly appeared peaks are indicated by arrow for the spectrum of the $U^{et}_{p}U$ DNA oligomer at a 0.7 molar ratio of HMGB1 A-box.

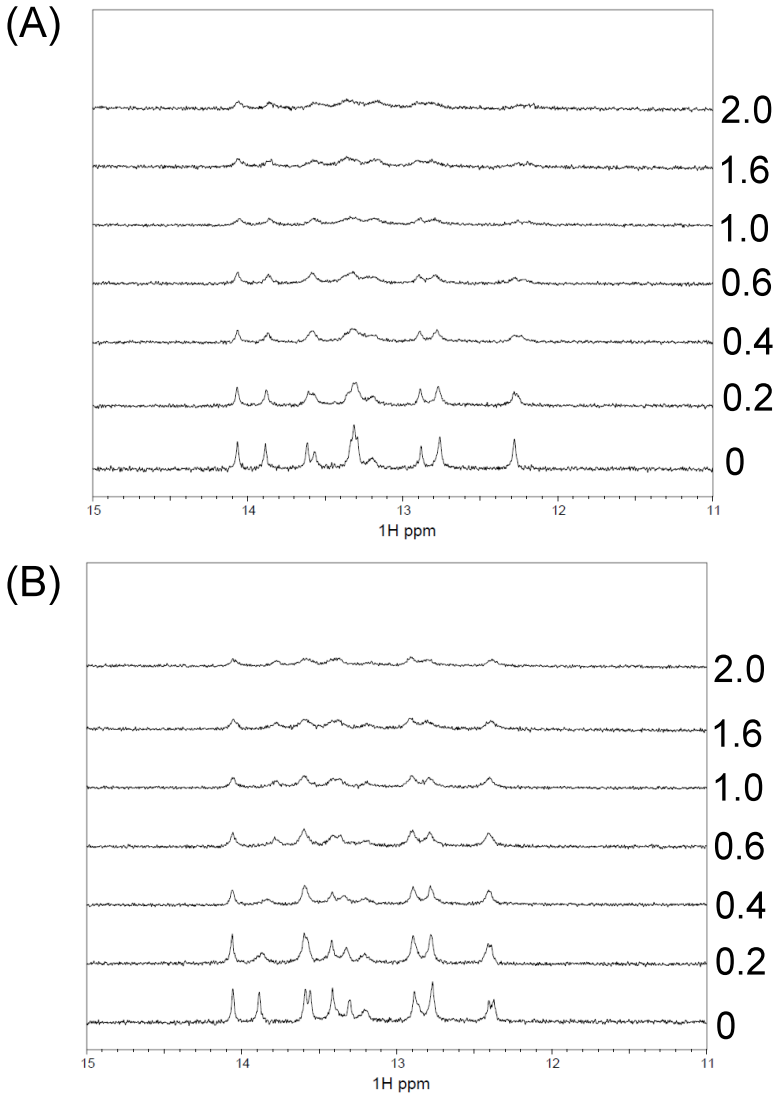

Appendix Figure 13. Titration experiments of the $U^{et}_{p}U$ (A) and $U^{pr}_{p}U$ (B) DNA oligomers with HMGB1 A-box (F38A). Molar ratios of HMGB1 A-box (F38A) to DNA oligomers are indicated on the right of spectra.

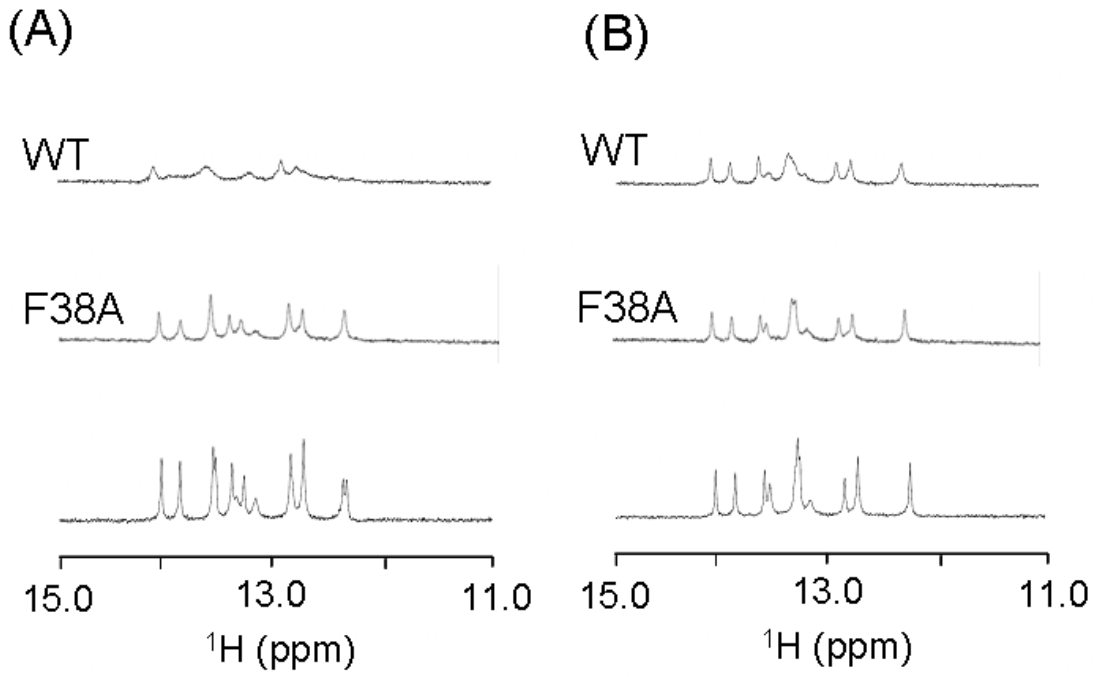

Appendix Figure 14. 1D 1-1 echo NMR spectra of the $U^{et}_{p}U$ (A) and $U^{pr}_{p}U$ (B) DNA oligomers without protein (bottom), with 2-fold amount of HMGB1 A-box (F38A) (middle), and with 2-fold amount of HMGB1 A-box (WT) (top).

whereas imino-proton peaks of the $U^{et}_{p}U$ DNA oligomer with an excess amount of HMGB1 A-box WT remained broad (Appendix Figure 14). These spectra indicate that (1) the binding affinity of the $U^{et}_{p}U$ DNA oligomer is higher than that of the $U^{pr}_{p}U$ DNA oligomer, (2) the binding affinity of the $U^{et}_{p}U$ DNA oligomer for HMGB1 A-box decreased by the F38A mutation in HMGB1 A-box, (3) for the F38A mutant, binding affinities of the $U^{et}_{p}U$ and $U^{pr}_{p}U$ DNA oligomers are similar. Thus Phe-38 is important for the binding of the $U^{et}_{p}U$ DNA oligomer to HMGB1 A-box, and may cause the difference in affinity of the $U^{et}_{p}U$ and $U^{pr}_{p}U$ DNA oligomers for HMGB1 A-box. In other words, the presence of the pocket is important for the interaction of alkylene cross-linked DNA oligomer with HMGB1 A-box. The pocket may be needed for strong interactions with Phe-38 of HMGB1 A-box.

6.4.2 Reason of the affinity difference; thermal stability

Although the structure of the $U^{et}_{p}U$ DNA oligomer is closer to that of the CP linked DNA oligomer complexed with HMGB1 A-box than the $U^{pr}_{p}U$ DNA oligomer, there are structural differences between the $U^{et}_{p}U$ DNA oligomer and the CP linked DNA oligomer complexed with HMGB1 A-box; the minor groove (Appendix Figure 7D), the bending angle (Appendix Table 2) and the pocket at cross-linked site (Appendix Figure 8) of the CP linked DNA oligomer is wider, deeper and larger than the $U^{et}_{p}U$ DNA oligomer, respectively. Therefore, the structure of the $U^{et}_{p}U$ DNA oligomer will change upon binding to HMGB1 A-box. The $U^{et}_{p}U$ DNA oligomer is less thermally stable than the $U^{pr}_{p}U$ DNA oligomer, as indicated by 1D and ^{1}H-^{1}H NOESY spectra at various temperatures (Appendix Figure 5 and 8). Hence, a structural change of the $U^{et}_{p}U$ DNA oligomer is considered to be easier than that of the $U^{pr}_{p}U$ DNA oligomer. This may be also involved in the difference in affinity for HMGB1 A-box between the $U^{et}_{p}U$ and $U^{pr}_{p}U$ DNA oligomers.

6.5 Conclusion

In this study, we have determined the solution structures of the $U^{et}_{p}U$ and $U^{pr}_{p}U$ DNA oligomers. Both DNA oligomers display right-handed B-form like structures moderately bended around the cross-linked site. However, local structures around the cross-linked sites are different between these DNA oligomers; the $U^{et}_{p}U$ DNA oligomer has a pocket at the cross-linked site, whereas the $U^{pr}_{p}U$ DNA oligomer does not. The pocket is presumably important for recruiting HMGB1 A-box by interacting with Phe-38 of HMGB1 A-box, and enhances binding of the $U^{et}_{p}U$ DNA oligomer to HMGB1 A-box (Appendix Figure 15).

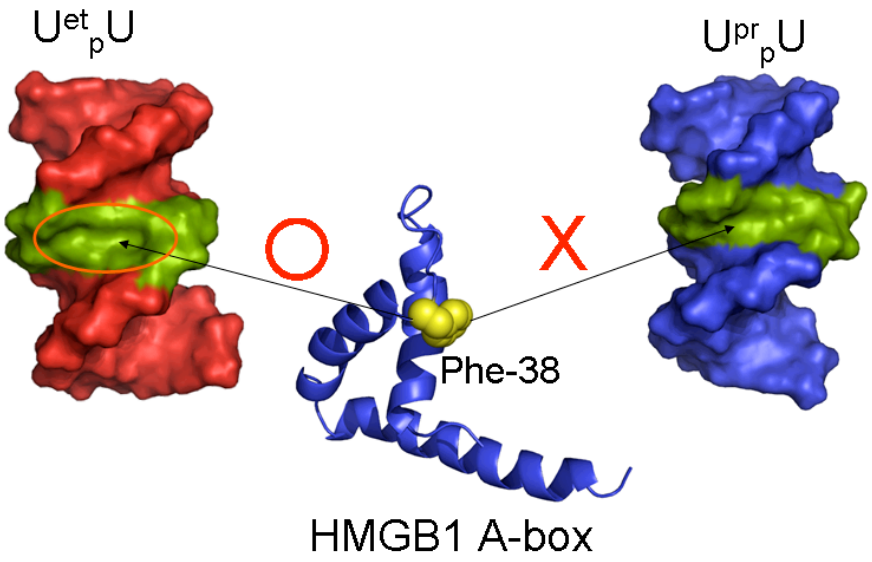

Appendix Figure 15. The DNA recognition mechanism by HMGB1 A-box.